Eur. Phys. J. B (2020) 93: 191
https://doi.org/10.1140/epjb/e2020-10143-1

THE EUROPEAN PHYSICAL JOURNAL B

Regular Article

Theoretical analysis of the structural, electronic, optical and thermodynamic properties of trigonal and hexagonal $Cs_3Sb_2I_9$ compound

Saadi Berri[1,2,a]

[1] Laboratory for Developing New Materials and Their Characterizations, University of Setif 1, Algeria
[2] Department of Physics, Faculty of Science, University of M'sila, Algeria

Received 18 March 2020 / Received in final form 9 July 2020 / Accepted 25 August 2020
Published online 5 October 2020

Abstract. The structural, electronic, optical and thermodynamic properties of $Cs_3Sb_2I_9$ compound with 0-D dimer form (hexagonal SP; $P63/mmc$, no. 194) and the 2-D layered form (trigonal SP; $P3\bar{m}1$, no. 164) phases have been investigated and reported using both FP-LAPW and PP-PW methods. Besides, the thermodynamic properties of the materials of interest have been studied using the quasi-harmonic Debye model accommodating the lattice vibrations effects. The obtained lattice parameters for dimer and layered phase reveal very good accord with experiment. The computed electronic band structures show that in the dimer phase the material of interest is an indirect band-gap (k–Γ) semiconductor, whereas it is a direct band-gap (Γ–Γ) in the layered phase. The semiconducting material $Cs_3Sb_2I_9$ of interest was found to be stable against volume change of 0 to +14%. Moreover, the optical properties of the material in question are also examined and discussed. The effect of pressure and temperature on the studied properties is found to be highly effective in tuning some of the macroscopic properties of the compound in question.

1 Introduction

Recently, with the fast-growing technological demands for multifunctional materials, halide perovskite received growing attention due to their interesting physical properties such as their application in solar cells [1,2] and light-emitting diodes(LEDs) [3].

An advantage of the halide perovskite family of compounds is that the properties are highly tunable with chemical composition [4]. Meanwhile, their excellent optoelectronic properties, defect tolerance, easy synthesis and cost effectiveness [5–8]. Furthermore, the power conversion efficiency of perovskite-based solar cells is now becoming comparable to that of silicon photovoltaics [9]. The first record of perovskite-based solar cell efficiency, however, was reported by Miyasaka et al. [10].

Cesium lead halide perovskite nanocrystals have attracted attention as a new class of exhibiting high photoluminescence quantum yields (PLQY), narrow emission [11] and tunable absorption/emission wavelengths [12] has accelerated the emergence and development of perovskite-based nanomaterials for applications such as light-emitting diodes (LEDs), [13] lasers, [14] and visible-light communication [15].

Recently, it has been predicted that the hybrid organometal trihalide perovskites (OTP) semiconductors possess strong spin–orbit coupling [16], and Rashba-type splitting [17] that originate from the heavy metal (Pb); this implies that (OTP) may also be considered for spintronics applications. As a matter of fact, spintronics is an emerging domain that will most likely have an important impact on the electronics aspects [18–24]. One of promising applications of spintronics is multiple-states memory devices, such as tunneling magneto-resistance and giant magneto-resistance, whose functions totally depend on magnetization and can only be realized by using spin direction [25].

The structural, electronic and thermodynamic properties of solid materials are important fundamental parameters for an accurate understanding of the physics of solid-state matter [26]. Under extreme conditions of temperature and pressure, the fundamental properties of solid materials behave in a manner different from that at normal conditions [27]. Thus, the knowledge of the new properties of materials obtained under high temperature and pressure is extremely useful for the technological applications of these materials at extreme conditions.

[a] e-mail: saadi.berri@univ-msila.dz

However, only a limited data has been reported on the fundamental properties of $Cs_3Sb_2I_9$ compound. This has motivated us to investigate on the structural, electronic, optic and thermodynamic properties of this material by performing the band structure calculations using the first principle methods. The remaining of the paper is organized as follows: the theoretical background is described in Section 2. Results are presented and discussed in Section 3. A summary of the results is given in Section 4.

2 Method of calculations

The experimental crystal parameters as reported by Yamada et al. [28] have been considered. $Cs_3Sb_2I_9$ compound crystallize in the 0-D dimer form (space group P63/mmc, no. 194, $Z = 2$) and the 2-D layered form ($P3\bar{m}1$, no. 164, $Z = 1$). The atomic coordinates for $Cs_3Sb_2I_9$ are illustrated in Appendix A. The crystal structures of $Cs_3Sb_2I_9$ compound is displayed in Figure 1. The calculations are performed as follows. The first-principles calculations are performed by employing the FP-LAPW method [29], as implemented in the WIEN2K code [30]. In the study of structural properties, the exchange correlation energy is treated within the GGA and Tran-Blaha modified beck Johnson (TB-mBJ) potentials [31]. In order to ensure convergence of the computed structures and energetic we use the value of plane wave cut-off $\mathrm{Rmt} \times \mathrm{Kmax} = 8$, the radii RMT of the muffin tins are chosen to be approximately proportional to the corresponding ionic radii. The maximum radial expansion $\mathrm{lmax} = 10$. The energy between the successive iterations is allowed to converge to 10^{-4} Ry and the forces are minimized to 1 mRy Bohr^{-1}. The Monkhorst–Pack special k-points were performed using 143 special k-points in the irreducible Brillouin zone for layered, and 90 k-points for the dimer phase. Calculations of the frequency-dependence of the optical properties were carried out using 285 and 176 k-points, respectively for the layered and dimer phases.

We have also used the non-local ultrasoft pseudopotential of the Vanderbilt-type [32] according to GGA-sol approach [33]. A computer program CASTEP (Cambridge Serial Total Energy Package) [34], was already used to calculate structural, electronic and optical properties of $Cs_3Sb_2I_9$. The kinetic cut-off energy for the plane wave expansion is taken to be 370 eV for all cases being considered here. The special k-point sampling for the integration of first Brillouin zone has been employed by using the Monkhorst–Pack method with $10 \times 10 \times 8$ and $11 \times 11 \times 7$ k-points for the layered and dimer phases, respectively. Based on the Broyden Fletcher Goldfarb Shenno (BFGS) [35] minimization technique, the system reached the ground state via self-consistent calculation when the total energy is stable to within 5×10^{-6} eV/atom

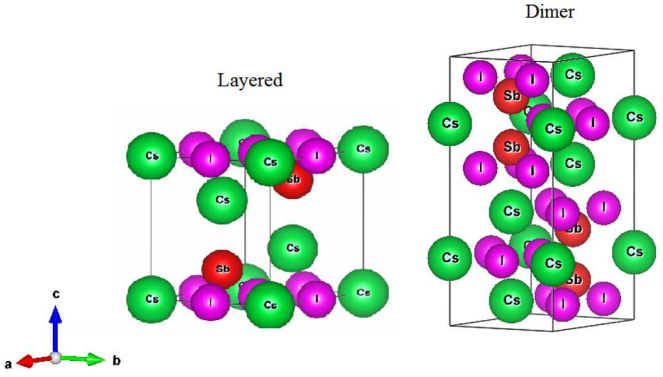

Fig. 1. Crystal structure for $Cs_3Sb_2I_9$.

the force is less than 10^{-2} eV/Å. To calculate the optical properties, dense Monkhorst–Pack special k-points were used. $20 \times 20 \times 16$ and $18 \times 18 \times 15$ special k-points mesh for the layered and dimer phases, respectively.

To investigate the thermodynamic properties of $Cs_3Sb_2I_9$ compound, the quasi-harmonic Debye model has been used [36]. Theoretical details of the model used are available in reference [37] and references therein.

3 Results and discussion

Our basic procedure in this work is to calculate the total energy as a function of the unit-cell volume around the equilibrium cell volume V_0 in both layered and dimer phases, using FP-LAPW and PP-PW methods. The optimized lattice parameters a (Å), c (Å), bulk modulus B and its pressure derivative B' at the equilibrium volume are obtained by fitting the total energy to Murnaghan's equation of state (EOS) [38]. Murnaghan's EOS is given by,

$$E(V) = E_0 + \frac{BV}{B'}\left[\frac{(V/V_0)^{B'}}{B'-1} + 1\right] - \frac{BV_0}{B'-1} \qquad (1)$$

where E_0 is the minimum energy, B is the bulk modulus at the equilibrium volume and B' is the pressure derivative of the bulk modulus. Pressure P and bulk modulus B are given by $p = -\frac{dE}{dV}$, $B = -V\frac{dP}{dV} = V\frac{d^2E}{dV^2}$. Figure 2 shows the total energy as a function of the unit-cell volume. This has allowed the determination of a (Å) and c (Å), B (GPa) and B'. The resulting structural parameters for $Cs_3Sb_2I_9$ compound being considered in the present work are listed in Table 1. The optimized ground state lattice parameters a (Å) and c (Å) are found in close agreement with the already available experimental data [28,39] and previous theoretical calculations [40]. The obtained lattice constants a (Å) and c (Å), bulk modulus B (GPa) and pressure derivative of bulk modulus B' are presented and compared with existing data in the literature in Table 1. Based on the experimental data, the equilibrium lattice constants a (Å) and c (Å) for dimer

Table 1. Lattice constant a (Å), c (Å), bulk modulus B (in GPa), first-pressure derivative of bulk modulus B' and energy band gap E_g (eV) for $Cs_3Sb_2I_9$ compound.

$Cs_3Sb_2I_9$		a (Å)	c (Å)	B (GPa)	B'	E_g (eV)
Dimer						
	FP-LAPW GGA	8.446	21.212	19.570	4.548	1.880
	PP-PW	8.682	21.763	55.213	–	2.001
	Exp [28]	8.349	20.916	–	–	–
	Exp [39]	8.39	20.936	–	–	–
	E_g^{opt} [41]	–	–	–	– 2.3	
	E_g^{opt} [42]	–	–	–	– 2.0	
	HSE [40]	–	–	–	–	2.40
Layered		–	–	–	–	–
	FP-LAPW	8.260	10.150	21.401	5.047	1.442
	PP-PW	8.764	10.521	69.673	–	1.547
	Exp [28]	8.420	10.386	–	–	–
	PAW(LDA) [40]	8.159	10.109	–	–	1.12
	PBE(GGA) [40]	8.661	10.625	–	–	1.55
	HSE [40]	8.639	10.618	–	–	2.06
	E_g^{opt} [41]	–	–	–	–	2.05
	E_g^{opt} [42]	–	–	–	–	1.89
	PBE(GGA) [43]	–	–	–	–	–
	HSE06 [43]	–	–	–	–	–
	PAW-PBE (GGA) [44]	8.664	10.633	–	–	2.04
	E_g(DFT/HSE06) [45]	–	–	–	–	(1.55/2.13)

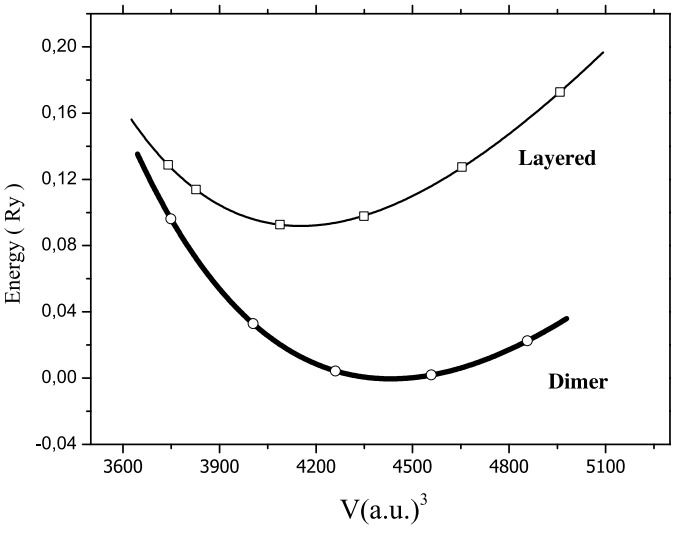

Fig. 2. Calculated normalized energy as a function of volume for $Cs_3Sb_2I_9$ compound. The total energies at their equilibrium lattice constants have been set at zero.

phase are best described by FP-LAPW, compared with the PP-PW method. Our results indicate that the dimer phase of $Cs_3Sb_2I_9$ is at its ground state. Moreover, the authors of reference [40] have computed the structural geometry of layered phase using Projector Augmented Wave (PAW) formalism as implemented in the VASP code [41]. We see that the bulk modulus is comparatively small (<100 GPa), thus $Cs_3Sb_2I_9$ can be regarded as medium hard material. To the best of our knowledge, there are no experimental or theoretical data reported for the bulk modulus and its pressure derivative for the material of interest, and hence our results are predictions.

The investigation of the electronic band structure and total density of states are important because most of the physical properties of solids are related to them. For that, the calculated band structure and total density of states (TDOS) at equilibrium volume of $Cs_3Sb_2I_9$ in its layered and dimer structures have been carried out using both FP-LAPW and PP-PW methods. Based on the lattice symmetry, the integration paths Γ–M–K–Γ–A–L–H–A are performed so as to treat the band structure for layered and dimer phases. At the equilibrium lattice constant of $Cs_3Sb_2I_9$, the calculations of the band structures have been done for both methods. The obtained results are displayed in Figure 3. The valence band maximum (VBM) is located at k-point for dimer, whereas the conduction band minimum (CBM) is located at Γ points. The energy gap obtained from FP-LAPW approach is 1.88 eV, while that obtained from PP-PW calculations is 2.001 eV (see Tab. 1). A good accord can be observed between our findings and the experimental [42,43]. One can note that the band gaps calculated using the PP-PW method gave the best agreement with experimentally reported values. In the case of layered phase, the (CBM) and the (VBM) are still at the same point Γ, which indicate their direct band gap behavior. The PBE calculated values of band gap (Γ-Γ) for FP-LAPW and PP-PW are 1.442 and 1.547 eV, respectively. The experimental value of the band gap for layered is 2.05 eV, obtained by using Tauc plot of the absorbance data [42]. While McCall et al. [43] found a band gap of 1.89 eV by using Bridgman method. The previous computational studies appear to give much values

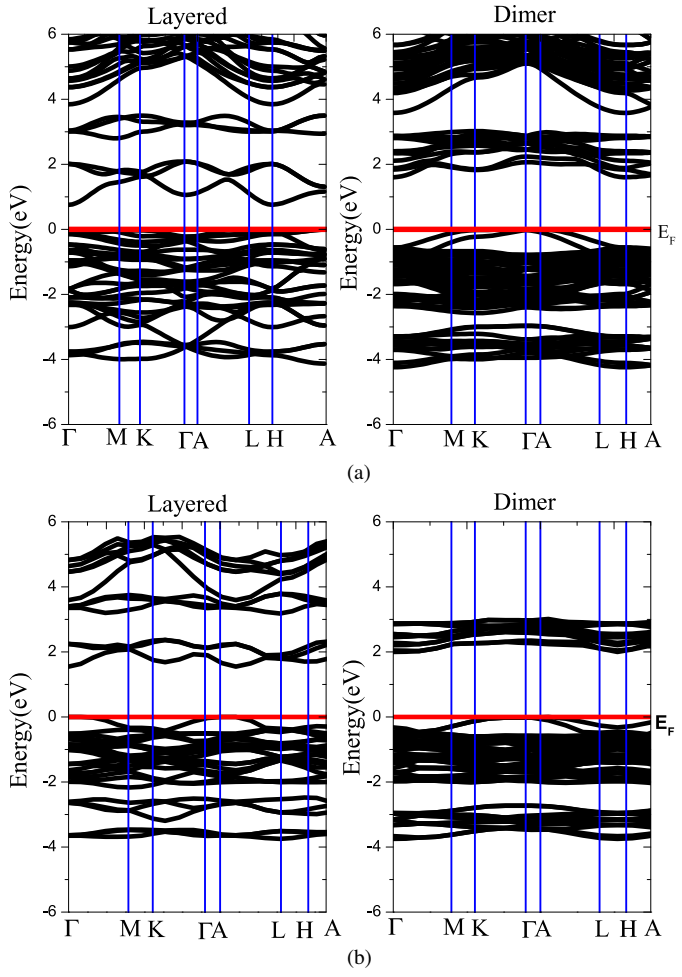

Fig. 3. Band structure for high-symmetry directions in the Brillouin zone using (a) FP-LAPW, (b) PP-PW methods.

than those found in the present work for both phases. It is worth noting that the computed energy band gaps of both phases being studied here are calculated better (as compared to experiment) when using the HSE approximation [40]. The disagreement of our results with respect to experiment is due to the use of GGA approach which is well known to underestimate the energy band gaps with respect to experiment. Moreover, the DFT results show several conduction bands with ∼0.5 eV separation, [44,45] all of which may contribute to the absorption. The perfect semiconductor behavior of $Cs_3Sb_2I_9$ has already been reported by Kresse and Joubert [46] using first-principles study. Thus, our results confirm those of reference [47]. To this point, $Cs_3Sb_2I_9$ semiconductor material has received great attention as a promising candidate for photovoltaic devices.

In order to get a deeper insight into the electronic structure of $Cs_3Sb_2I_9$, the total (TDOS) and partial atomic densities of states (PDOS) have been calculated in both method. Because of the similarity in the most results, only FP-LAPW results are presented (See Fig. 4). The Fermi level is set to be 0 eV. As can be seen from Figure 4, the DOS can be divided into three parts, at lower energy where we find the contribution of I s, Cs $px + py$ and pz and Sb s states; the second part is from −0 to 0 eV that is mainly derived from I pz , I $px + py$ and I d states with a small contribution Sb pz, the third part which is beyond the Fermi level, where the contribution is due to pz and $px + py$ of Sb atoms.

Meanwhile, the electronic structure has also been computed versus pressure and plotted in Figure 5. We observe a clear shift of the Fermi level. Nevertheless, one can note a preserved semiconducting nature for both band structures of interest in the stress range of 0–14%.

The degree of polarization of a material when it is under an external electric field is described by the real part of the dielectric function is described by the real part of the dielectric function. The imaginary part of the dielectric function shows the amount of absorption inside the material under load. It contributes into both intra-band and inter-band transitions. Nevertheless, the intra-band transition contribution is only significant for metals. Besides, the inter-band transition can be further split into direct and indirect transitions. The indirect inter-band transitions that involve phonons scattering are expected to have only a little contribution to the imaginary part of the dielectric function and hence are neglected. In Figure 6, we present the dielectric function of $Cs_3Sb_2I_9$ as calculated by FP-LAPW and PP-PW methods. Note that the values of the dielectric function of the material of interest are large within near and middle ultraviolet regions. Our analysis of the $\varepsilon_2^{xx}(\omega)$ and $\varepsilon_2^{zz}(\omega)$ spectra shows that the threshold energy (first critical point) of the dielectric function occurs at about 1.89 and 2.06 eV for dimer phase (Fig. 6a), while in layered phase (Fig. 6b) it occurs at 0.92 and 1.55 eV for FP-LAPW and PP-PW methods, respectively. These points are mainly coming from the electron transition from the I pz (VB) to Sb pz (CB) orbitals. The peaks are positioned at A1, A2, A3, A4, A5 and A6, respectively. These points come essentially from the transition of electrons between the three levels of the valence band and the two levels of the conduction band (see Tab. 2). Therefore, the optimal working regions of the device lie in the visible–ultraviolet regions that make these materials more suitable for optoelectronic applications.

On the other hand, it is observed from Figure 6, that the real parts of the dielectric function $\epsilon_1(\omega)$ is extended in the energy range of 2–5.2 and 1–4.7 eV, for the dimer and layered phases, respectively. Furthermore, the imaginary part of the dielectric function $\varepsilon_2(\omega)$ is calculated with the sharp peaks of 2.62 (3.83) and 1.41(2.02) as calculated by FP-LAPW(PP-PW) methods in energy ranges of 1.1–6.2 eV, for the dimer and layered phases, respectively. High value of the real part $\epsilon_1(\omega)$ spectra in the visible and ultraviolet energy ranges indicates that these materials can be efficiently applied in optoelectronics domain.

From the dispersion curves of calculated dielectric constant and refractive index, the calculated dielectric

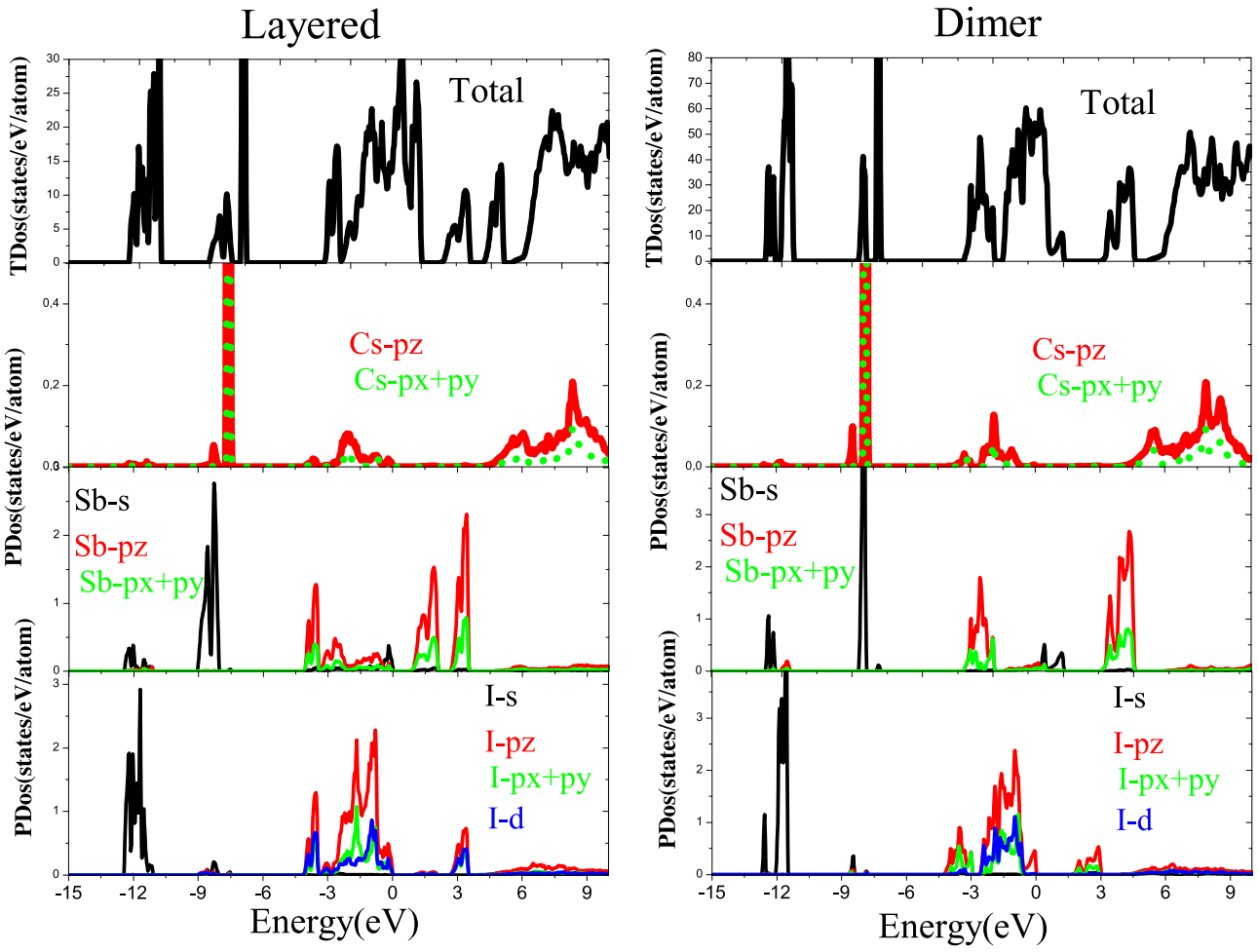

Fig. 4. Total and projected density of states for $Cs_3Sb_2I_9$ using FP-LAPW method.

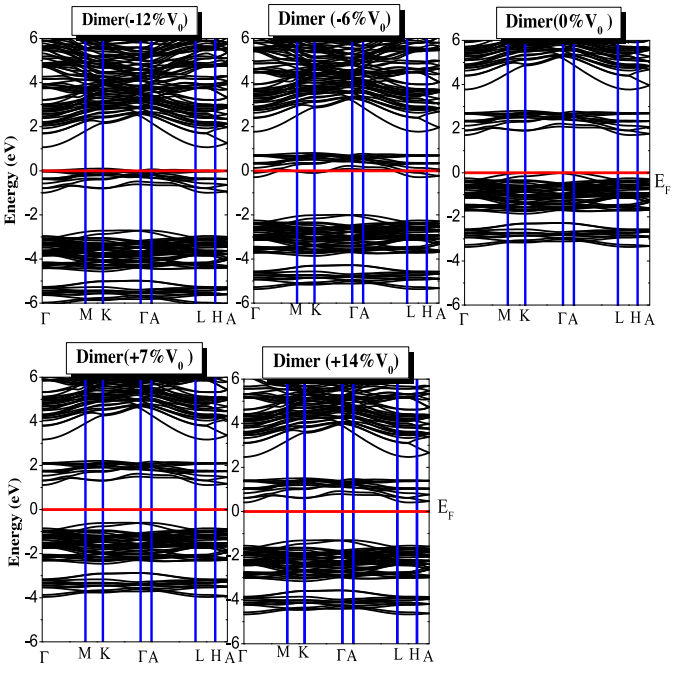

Fig. 5. Band structure under pressure effect.

constant $\varepsilon_1^{xx}(0)$ and $\varepsilon_1^{zz}(0)$ and the static refractive index $n^{xx}(0)$ and $n^{zz}(0)$ of $Cs_3Sb_2I_9$ compound using FP-LAPW and PP-PW methods are reported in Table 3.

The refractive index $n(\omega)$ is a quantity that describes how much light is refracted after entering a material [48]. The calculated value of refractive index $n(\omega)$ and the extinction coefficient $K(\omega)$ with the variation of wavelength is displayed in Figure 7. From the refractive index plot, we remark that the material possesses high refractive index within microwave region and decreases at higher energy in the ultraviolet lointain. It is clearly seen that the calculated spectra show pronounced peaks originating from the excitonic transitions at the E0 edges. The strongest peaks in $n(\omega)$ spectra are related mainly to the 2-D excitontransition (E1) [49]. Furthermore, after 4.5 eV within ultraviolet moyen region the velocity of light is greater than the light celerity because $n(\omega) \approx 1$. From Figure 7, one can note that the material in question has strong extinction effects that occur near the ultraviolet region. These effects are reduced when increasing the photon energy.

The optical absorption coefficients for $Cs_3Sb_2I_9$ with both layered and dimer structures have been calculated

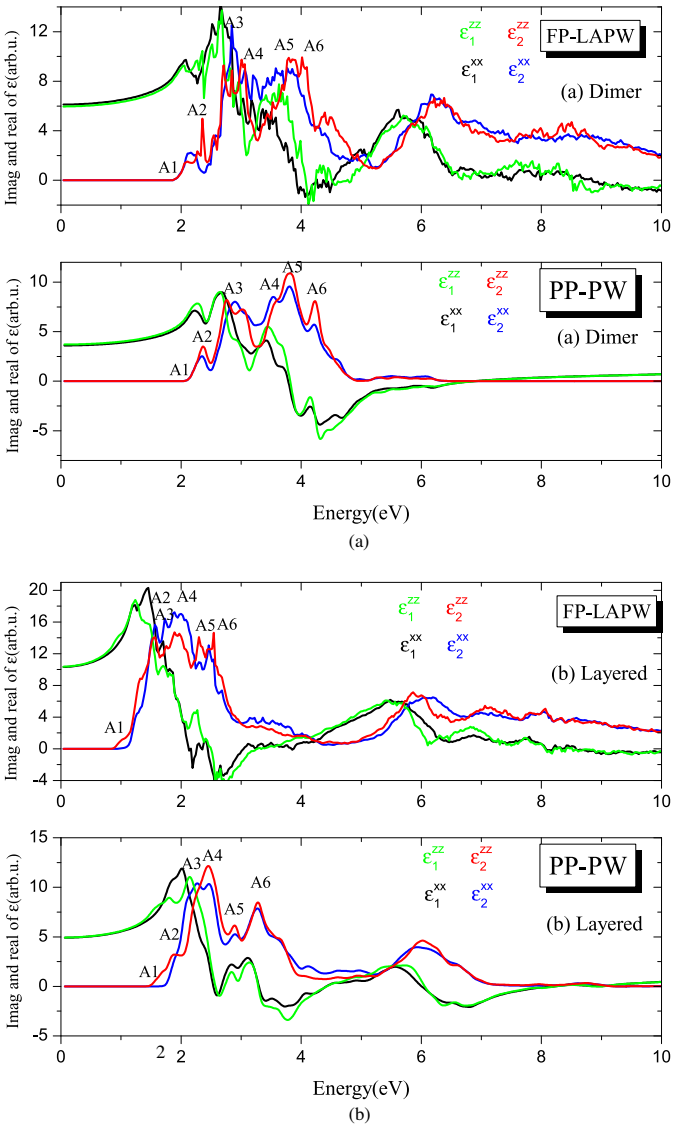

Fig. 6. The real part $\varepsilon_1(\omega)$ and imaginary part $\varepsilon_2(\omega)$ of dielectric constant $\varepsilon(\omega)$ for (a) dimer and (b) layered.

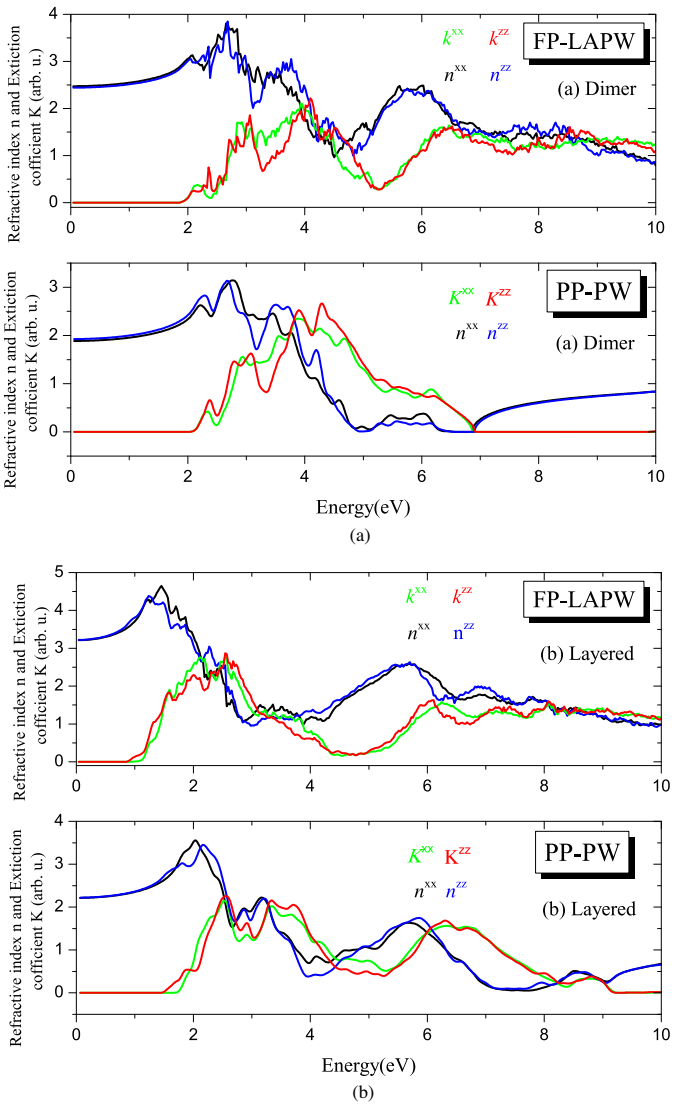

Fig. 7. Calculated refractive index $n(w)$ and extinction coefficient $k(w)$ for (a) dimer and (b) layered.

based on the electronic structures (see Fig. 8) Comparing the absorption curve in Figure 8 and Im–$\varepsilon(\omega)$ in Figure 5, it is observed that most of the absorbed light passes through the material or is used up on the electron transitions. Meanwhile, an onset energy of about 1.0 eV and for 1.8 eV, respectively for the layered and dimer phase.

The electron energy loss spectra give valuable information about intra- and interband transition and Plasmon excitation. The Eloss diagram in Figure 9 by the FP-LAPW and PP-PW calculation shows that there is no graph in the gap region as expected. The peaks shown in Figure 9 are the characteristics that are linked to the plasma resonance (PR) with a frequency known as ωp. The latter is defined as the bulk plasma frequency and occurs at $\varepsilon_1(\omega) = 0$ and $\varepsilon_2(\omega) < 1$ [50,51]. This suggests that there is a quick reduction in the reflectance. At the vacuum ultraviolet (VUV) edge, most of the amount of loss function (Loss) is occurred. But the maximum Loss values is occurred in the range of 6–8 eV for PP-PW and 18–20 eV for FP-LAPW methods, and also, we see severe anisotropy in this area by both methods.

In the next stage, we presented the thermodynamic properties of $Cs_3Sb_2I_9$ compound under high temperature and high pressure, we apply the quasi-harmonic Debye approximation. As a first step, a set of total energy calculations versus primitive cell volume (E–V) is carried out using the static approximation. The results are then fitted with a numerical EOS in order to determine the structural parameters at $P = 0$ and $T = 0$ and to derive the macroscopic properties as a function of pressure and temperature from standard thermodynamic relations.

The diagrams showing the volume unit cell-temperature at various pressures and lattice parameter-pressure at different temperatures for dimer and layered phase are

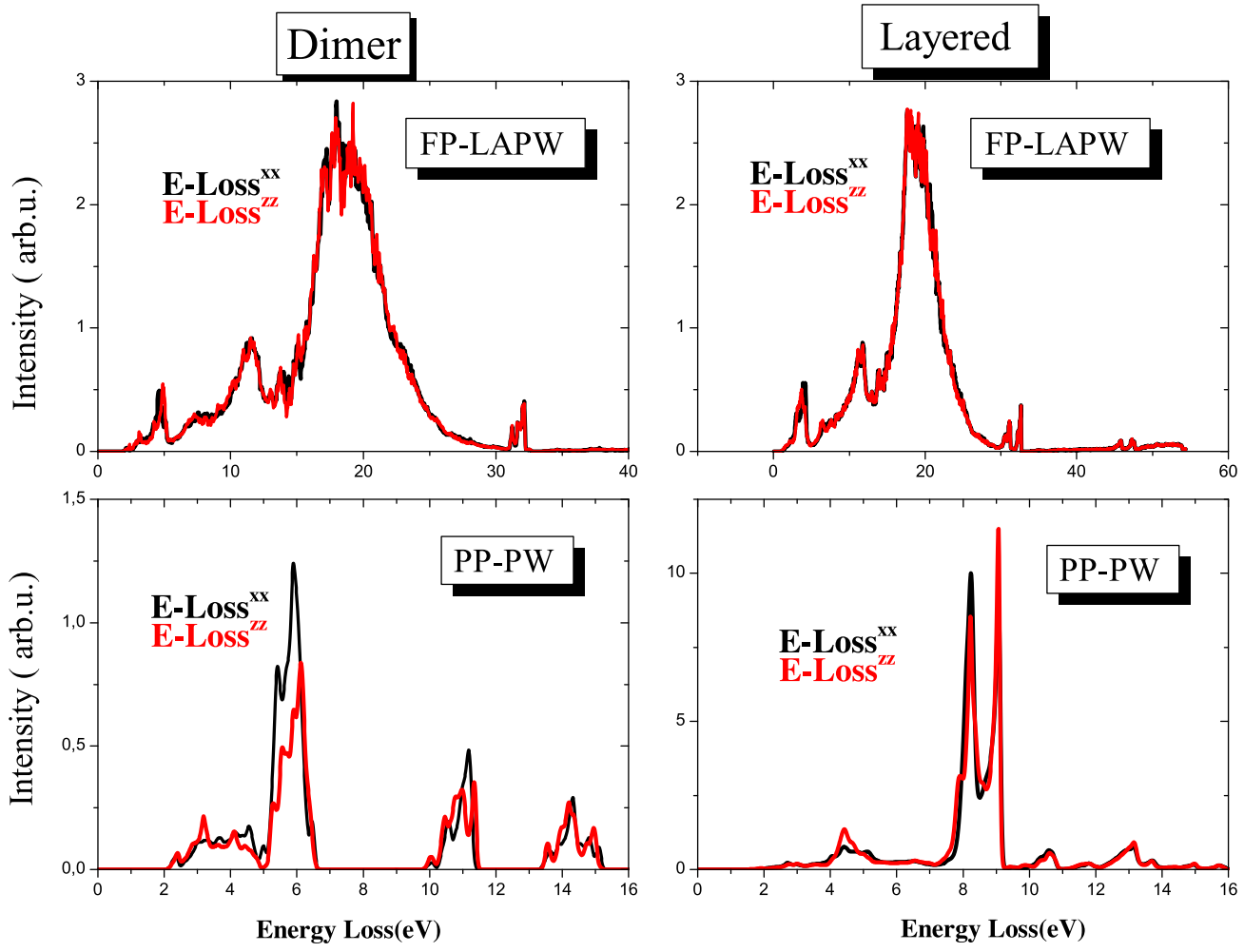

Fig. 8. Energy loss function $L(\omega)$ at the equilibrium lattice constants.

Table 2. Calculated plasma resonance (PR), static dielectric $\varepsilon_1^{xx}(0)$, $\varepsilon_1^{zz}(0)$, static refractive index $n^{xx}(0)$ and $n^{zz}(0)$ for $Cs_3Sb_2I_9$ compound.

Dimer	A1		A2		A3	
	FP-LAPW	PP-PW	FP-LAPW	PP-PW	FP-LAPW	PP-PW
	1.89	2.06	2.36	2.35	2.7	2.74
Transitions	I $pz \rightarrow$ Sb pz		I $px+py \rightarrow$ Sb pz		I $d \rightarrow$ Sb pz	
	A4		A5		A6	
	FP-LAPW	PP-PW	FP-LAPW	PP-PW	FP-LAPW	PP-PW
	3.32	3.49	3.6	3.79	4.01	4.23
Transitions	I $pz \rightarrow$ Sb $px+py$		I $px+py \rightarrow$ Sb $px+py$		I $d \rightarrow$ Sb $px+py$	
Layered						
	A1		A2		A3	
	FP-LAPW	PP-PW	FP-LAPW	PP-PW	FP-LAPW	PP-PW
	1.45	1.55	1.53	1.90	1.75	2.24
Transitions	I $pz \rightarrow$ Sb pz		I $px+py \rightarrow$ Sb pz		I $d \rightarrow$ Sb pz	
	A4		A5		A6	
	FP-LAPW	PP-PW	FP-LAPW	PP-PW	FP-LAPW	PP-PW
	1.99	2.74	2.30	2.89	2.84	3.28
Transitions	I $pz \rightarrow$ Sb $px+py$		I $px+py \rightarrow$ Sb $px+py$		I $d \rightarrow$ Sb $px+py$	

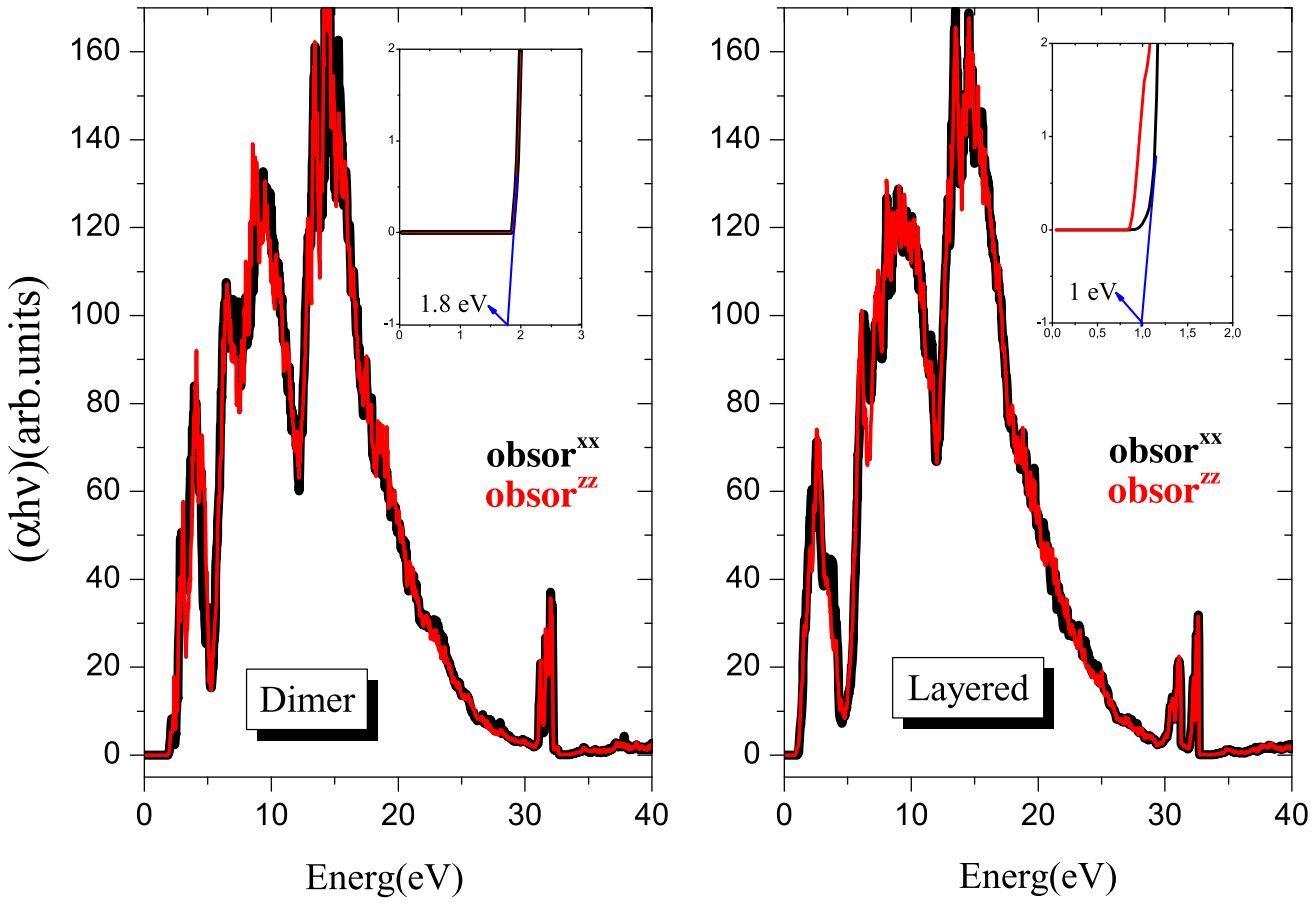

Fig. 9. Calculated absorption coefficients for $Cs_3Sb_2I_9$ using FP-LAPW method.

Table 3. Calculated plasma resonance (PR), static dielectric, static refractive index, for $Cs_3Sb_2I_9$ compound.

Phases		This work (FP-LAPW)	This work (PP-PW)
Dimer	PR	17.87	5.90
	$\varepsilon_1^{xx}(0)$	6.12	3.60
	$\varepsilon_1^{zz}(0)$	5.96	3.70
	$n^{xx}(0)$	2.47	1.88
	$n^{zz}(0)$	2.44	1.92
Layered	PR	18.17	8.16
	$\varepsilon_1^{xx}(0)$	10.32	4.91
	$\varepsilon_1^{zz}(0)$	10.36	4.93
	$n^{xx}(0)$	3.21	2.22
	$n^{zz}(0)$	3.22	2.21

plotted in Figure 10. We observe that for a given pressure, the volume unite cell increases monotonically with increasing temperature. Nevertheless, the rate of increase appears to be very moderate. On the other hand, for a given temperature, the volume unit cell is reduced when enhancing pressure. In the present contribution, the calculated volumes for dimer and layered phase at zero pressure and room temperature are found to be 4443.87 and 4164.28 (u.a.)^3, respectively.

The temperature dependence of B at various pressures for dimer and layered phase is displayed in Figure 11. Note that B varies in a quasi-linear way with temperature. This is true for all pressures in the interval 0–15 GPa. As a matter of fact, B decreases monotonically and very moderately when the temperature is increased. At room temperature and zero pressure, our results yielded values of B of 76.44 and 83.10 GPa GPa for dimer and layered phase, respectively. These values are in reasonably good accord with those obtained in the current work using PP-PW method (see Tab. 1).

The variation of the heat capacity at a constant volume C_V as a function of temperature at various pressures ranging from 0 to 15 GPa for dimer and layered phases is shown in Figure 12. We observe that C_V augments at elevated temperatures. The behavior seems to be quick at low temperatures but becomes slower at elevated temperatures. For temperatures less than 500 K, C_V depends on both temperature and pressure. At high temperatures, C_V approaches approximately 348.42 and 348.61 J mol^{-1} K^{-1}, respectively for dimer and layered phase.

The plot of the heat capacity at a constant volume C_V versus temperature at various pressures in the interval 0–15 GPa for dimer and layered phase is illustrated in Figure 9. We remark that C_V augments at elevated temperatures. The behavior seems to be quick at low temperatures but becomes slower at higher temperatures. For

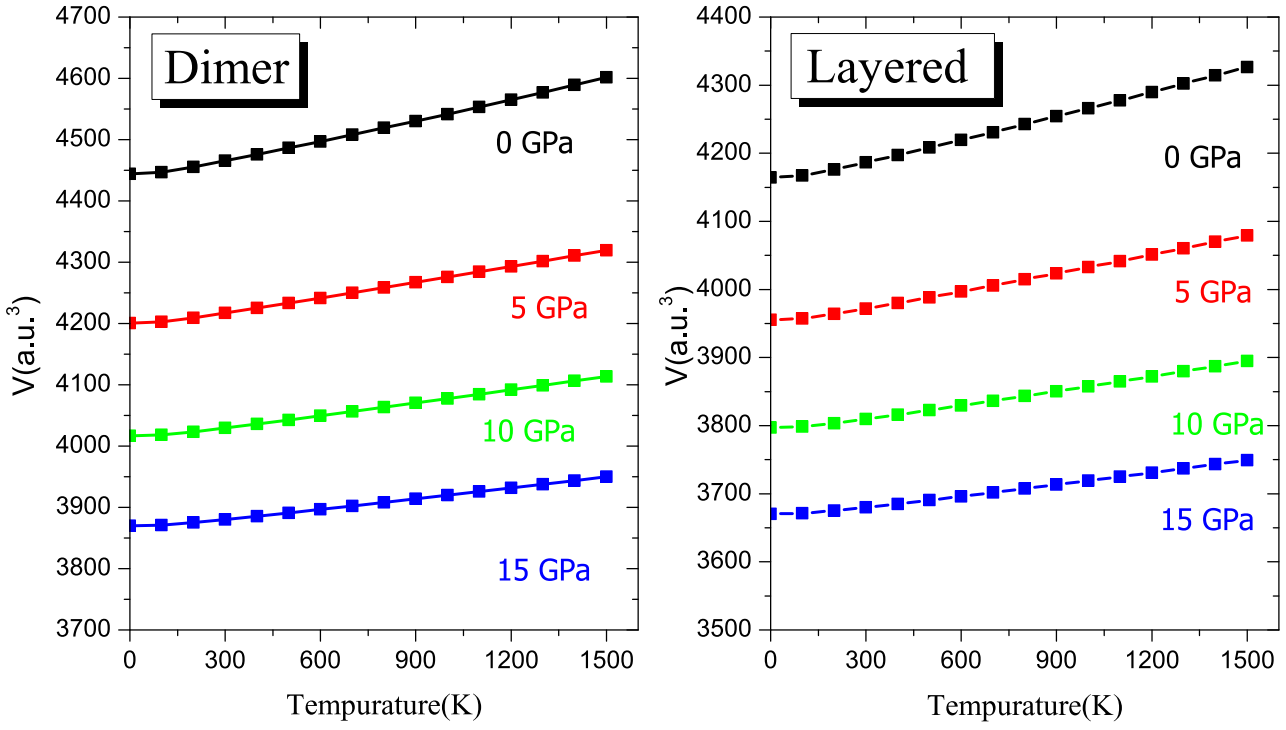

Fig. 10. Temperature dependence of the volume at various pressures.

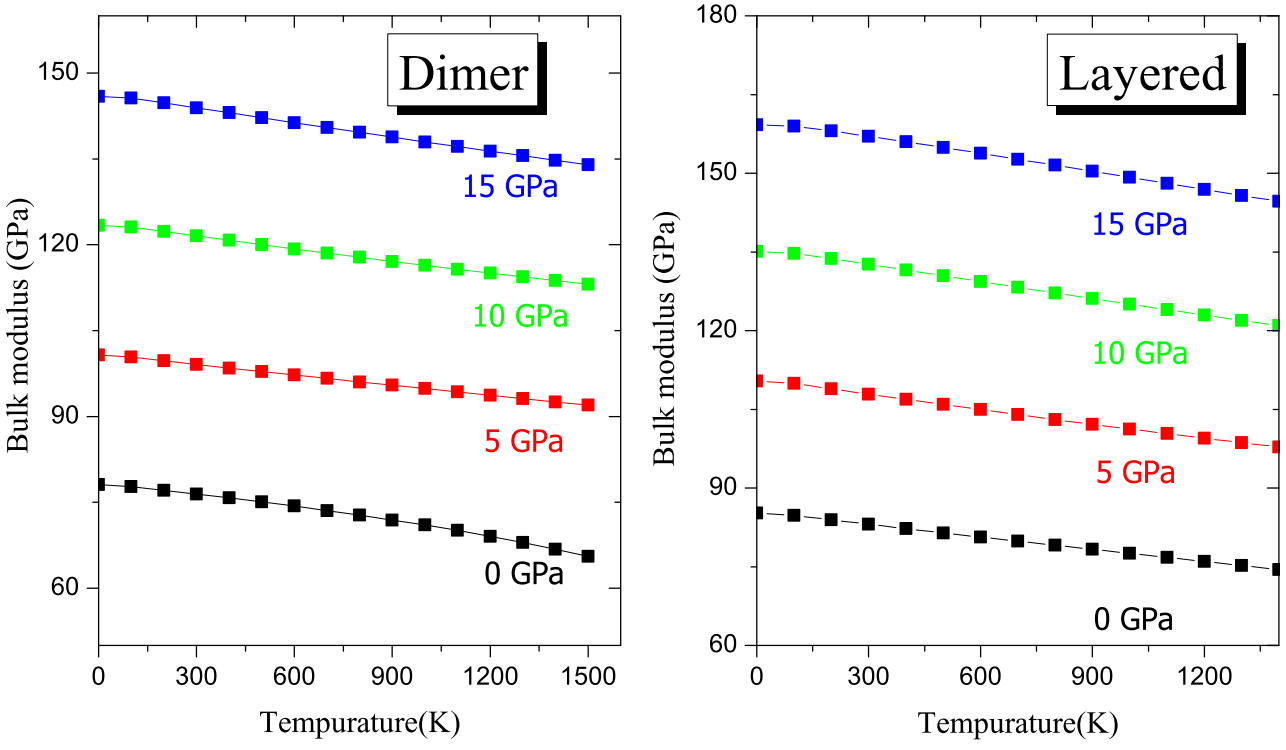

Fig. 11. Temperature dependence of the bulk modulus B at various pressures.

temperatures less than 400 K, C_V depends on both temperature and pressure. The behavior seems to be quick at low temperatures but becomes slower at higher temperatures. For temperatures less than 400 K, C_V depends on both temperature and pressure. At high temperatures, C_V approaches approximately 304.21 and 337.04 J mol^{-1} K^{-1}, respectively for dimer and layered phases. The details in the change appear to depend on pressure. The behavior of

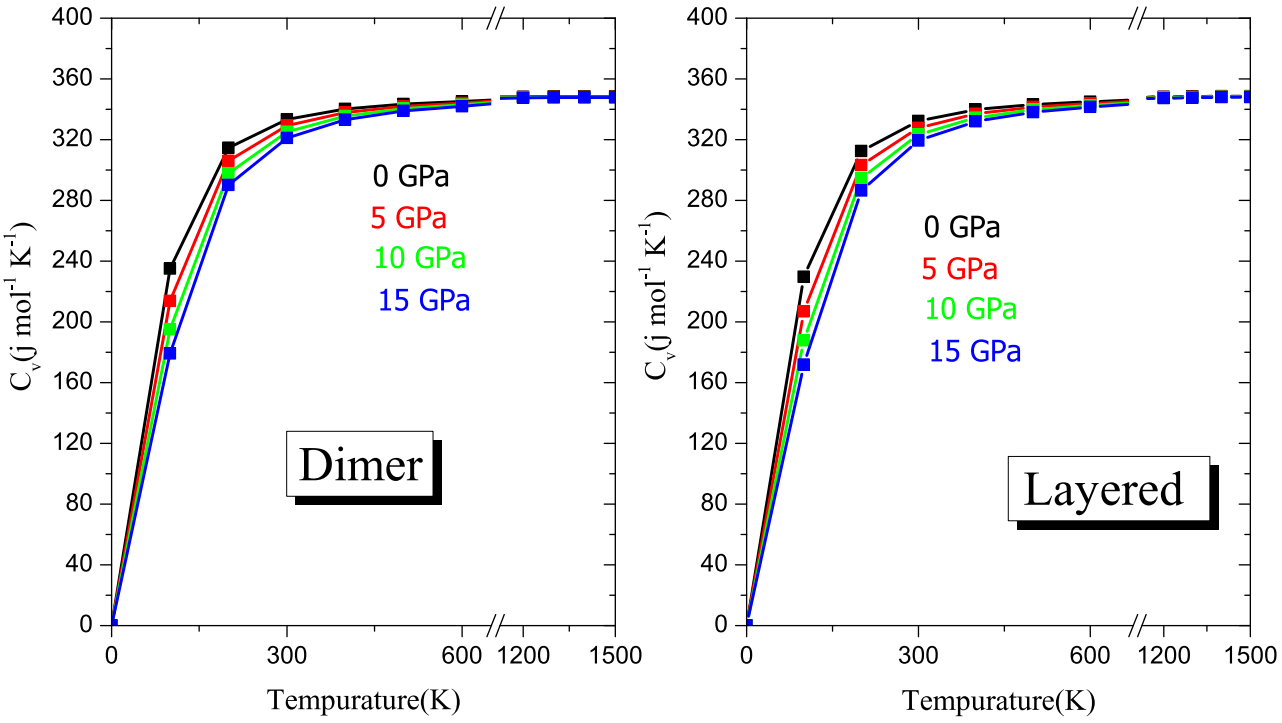

Fig. 12. Variation of the heat capacities C_V with temperature at various pressures.

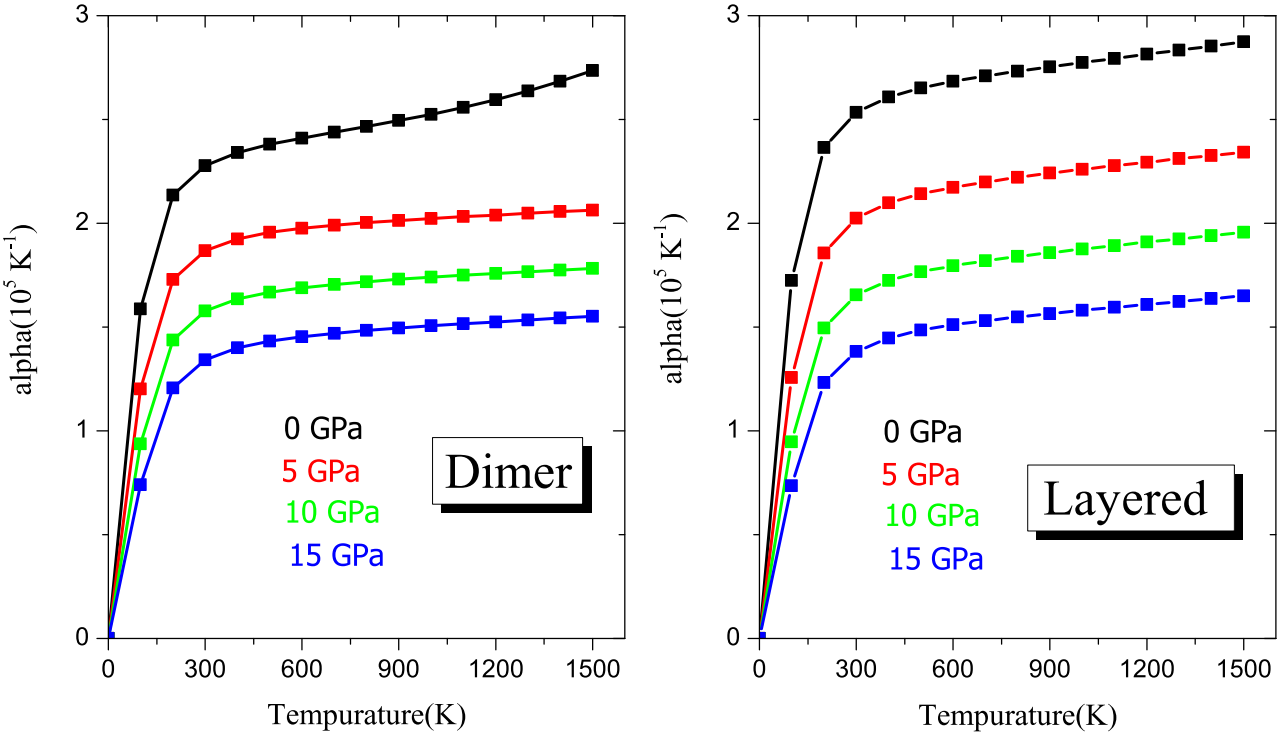

Fig. 13. Thermal expansion coefficient versus α versus temperature at different pressures.

C_V for all compounds of interest exhibits similar features in a wide range of pressures and temperatures.

The temperature dependence of the thermal expansion coefficient a of the dimer and layered phase at various pressures are depicted in Figure 13; it is clear that below 400 K, the thermal expansion coefficient increases rapidly, whereas at temperatures higher than 400 K, the a value initially remains constant and then increases linearly at

high pressure. At zero pressure and $T = 300$ K, a takes the values of 2.28×10^{-5} and $2.53 \times 10^{-5}\,\mathrm{K}^{-1}$ for dimer and layered phase, respectively.

4 Conclusion

Using the FP-LAPW and PP-PW methods where the exchange–correlation potential was calculated with the frame of $Cs_3Sb_2I_9$, we have analyzed the structural, electronic and optical properties of $Cs_3Sb_2I_9$ for both dimer form layered phases. Special attention was given to the effect of temperature and pressure on these features. The obtained lattice parameters for dimer form layered phase reveal very good accord with experiment. The computed electronic band structures show that in the dimer phase the material of interest is an indirect band-gap (k-Γ) semiconductor, whereas it is a direct band-gap (Γ–Γ) in the layered phase. The semiconducting materials $Cs_3Sb_2I_9$ of interest were found to be stable against volume change of 0 to +14%. Moreover, the optical properties of the material in question are also examined and discussed. The thermal effects on the macroscopic properties of the $Cs_3Sb_2I_9$ compound of interest were predicted and discussed using the quasi-harmonic Debye model in which the lattice vibrations were taken into consideration.

Appendix A:

Table A. Atomic coordinates for $Cs_3Sb_2I_9$ compound.

	Atom	Site	X	Y	Z
Dimer	Cs	2b	0	0	0.25
	Cs	4f	0.3333	0.6667	0.0850
	Sb	4f	0.3333	0.6667	0.8453
	I	6h	0.4929	0.9858	0.25
	I	12k	0.1653	0.3306	0.9189
Layered	Cs	1a	0	0	0
	Cs	2 d	0.6667	0.3333	0.672
	Sb	2 d	0.6667	0.3333	0.196
	I	3 e	0.5	0.5	0
	I	6 i	0.149	0.851	0.646

References

1. M.A. Green, A. Ho-Baillie, H.J. Snaith, Nat. Photonics **8**, 506 (2014)
2. S.D. Stranks, H.J. Snaith, Nat. Nanotechnol. **10**, 402 (2015)
3. D.W. de Quilettes, S. M. Vorpahl, S.D. Stranks, H. Nagaoka, G.E. Eperon, M.E. Ziffer, H.J. Snaith, D.S. Ginger, Science **348**, 683 (2015)
4. R.X. Yang, K.T. Butler, A. Walsh, J. Phys. Chem. Lett. **6**, 5014 (2015)
5. J. Lin et al., Nat. Mater. **17**, 261 (2018)
6. A. Marchioro, J. Teuscher, D. Friedrich, M. Kunst, R. van de Krol, T. Moehl, M. Grätzel, J.-E. Moser, Nat. Photonics **8**, 250 (2014)
7. Q. Lin, A. Armin, R.C.R. Nagiri, P.L. Burn, P. Meredith, Nat. Photonics **9**, 106 (2014)
8. O. Malinkiewicz, A. Yella, Y.H. Lee, G.M. Espallargas, M. Graetzel, M.K. Nazeeruddin, H.J. Bolink, Nat. Photonics **8**, 128 (2013)
9. M. Saliba et al., Science **354**, 206 (2016)
10. A. Kojima, K. Teshima, Y. Shirai, T. Miyasaka, J. Am. Chem. Soc. **131**, 6050 (2009)
11. Begum, R. Parida, M.R. Abdelhady, A.L. Murali, B. Alyami, N.M. Ahmed, G.H. Hedhili, M.N. Bakr, O.M. Mohammed, J. Am. Chem. Soc. **139**, 731 (2017)
12. M. Zirak, M. Zirak, M. Zirak, E. Moyen, H. Alehdaghi, A. Kanwat, W.-C. Choi, J. Jang, J. Am. Chem. Soc. **137**, 10276 (2015)
13. A. Swarnkar, A.R. Marshall, E.M. Sanehira, B.D. Chernomordik, D.T. Moore, J.A. Christians, T. Chakrabarti, J.M. Luther, Science **354**, 92 (2016)
14. S. Yakunin, L. Protesescu, F. Krieg, M.I. Bodnarchuk, G. Nedelcu, M. Humer, G. De Luca, Fiebig, M. Heiss, W. Kovalenko, M.V. Kovalenko, Nat. Commun. **6**, 8056 (2015)
15. I. Dursun, C. Shen, Parida, M.R. Pan, J. Sarmah, S.P. Priante, D. Alyami, N. Liu, J. Saidaminov, M.I. Alias, M.S. Abdelhady, A.L. Ng, T.K. Mohammed, O.F. Ooi, B.S. Bakr, O.M. Bakr, ACS Photonics **3**, 1150 (2016)
16. K. Tanakaa, T. Takahashia, T. Bana, T. Kondoa, K. Uchidab, N. Miura, Solid State Commun. **127**, 619 (2003)
17. M. Kim, J. Im, A.J. Freeman, J. Ihm, H. Jin, Proc. Natl. Acad. Sci. U.S.A. **111**, 6900 (2014)
18. Y. Han, R. Khenata, T. Yang, X. Wang, Results Phys. **13**, 102301 (2019)
19. T. Yang, R. Khenata, H. Khachai, X. Wang, Results Phys. **13**, 102331 (2019)
20. X. Wang, H. Khachai, R. Khenata, Superlatt. Microstruct. **130**, 472 (2019)
21. X. Wang, Z. Cheng, H. Khachai, R. Khenata, T. Yang, J. Solid State Chem. **276**, 352 (2019)
22. S. Berri, J. Magn. Magn. Mater. **385**, 124 (2015)
23. S. Berri, J. Sci.: Adv. Mater. Devices **3**, 254 (2018)
24. S. Berri, N. Bouarissa, M. Attallah, J. Supercond. Nov. Magn. **33**, 1737 (2020)
25. Y. Kajiwara, K. Harii, S. Takahashi, J. Ohe, K. Uchida, M. Mizuguchi, H. Umezawa, H. Kawai, K. Ando, K. Takanashi, S. Maekawa, E. Saitoh, Nature **464**, 262 (2010)
26. L. Bai, Y. Xue, Z. Cui, Thermochim. Acta **658**, 101 (2017)
27. C.C. Rinzler, A. Allanore, Philos. Mag. **97**, 561 (2017)
28. K. Daviau, K.K.M. Lee, Crystals **8**, 217 (2018)
29. P. Blaha, K. Schwarz, P. Sorantin, S.B. Trickey, Comput. Phys. Commun. **59**, 399 (1990)
30. P. Blaha, K. Schwarz, G. Madsen, D. Kvasnicka, J. Luitz, WIEN2K package, http://www.wien2k.at
31. F. Tran, P. Blaha Phys. Rev. Lett. **102**, 226401 (2009)
32. D. Vanderbilt, Phys. Rev. B **41**, 7892 (1990)
33. J.P. Perdew, A. Ruzsinszky, G.I. Csonka, O.A. Vydrov, G.E. Scuseria, L.A. Constantin, X. Zhou, K. Burke, Phys. Rev. Lett. **100**, 136406 (2008)

34. M.D. Segall, P.J.D. Lindan, M.J. Probert, C.J. Pickard, P. Hasnip, S.J. Clark, M.C. Payne, J. Phys.: Condens. Matter **14**, 2717 (2002)
35. T.H. Fischer, J. Almlof, J. Phys. Chem. **96**, 9768 (1992)
36. M.A. Blanco, E. Francisco, V. Luana, Comput. Phys. Commun. **158**, 7 (2004)
37. S. Berri, J. Sci.: Adv. Mater. Devices **4**, 319 (2019)
38. F.D. Murnaghan, Proc. Natl. Acad. Sci. U.S.A. **3**, 244 (1944)
39. B. Chabot, E. Parthé, Acta Cryst. B **34**, 645 (1978)
40. B. Saparov, F. Hong, J.-P. Sun, H.-S. Duan, W. Meng, S. Cameron, I.G. Hill, Y. Yan, D.B. Mitzi, Chem. Mater. **27**, 5622 (2015)
41. G. Kresse, J. Furthmüller, Comput. Mater. Sci. **6**, 15 (1996)
42. A. Singh, K.M. Boopathi, A. Mohapatra, Y.F. Chen, G. Li, C.W. Chu, ACS Appl. Mater. Interfaces **10**, 2566 (2018)
43. K.M. McCall, C.C. Stoumpos, S.S. Kostina, M.G. Kanatzidis, Wessels, B.W. Strong, Chem. Mater. **29**, 4129 (2017)
44. A. Koliogiorgos, S. Baskoutas, I. Galanakis, Comput. Condens. Matter **14**, 161 (2018)
45. Y.L. Liu, C.L. Yang, M.S. Wang, X.-G. Ma, Y.-G. Yi , J. Mater. Sci. **54**, 4732 (2019)
46. A. Jain, O. Voznyy, E.H. Sargent. J. Phys. Chem. C **121**, 7183 (2017)
47. K.M. McCall et al., ACS Photonics **5**, 3748 (2018)
48. T. Geng, Z. Ma, Y. Chen, Y. Cao, P. Lv, N. Li, G. Xiao, Nanoscale **12**, 1425 (2020)
49. S. Berri, Chin. J. Phys. **55**, 2476 (2017)
50. S. Berri, D. Maouche, N. Bouarissa, Y. Medkour, Mater. Sci. Semicond. Process. **16**, 1439 (2013)
51. R. Saniz, L.-H. Ye, T. Shishidou, A.J. Freeman, Phys. Rev. B **74**, 014209 (2006)

Journal of Science: Advanced Materials and Devices 5 (2020) 378–384

Contents lists available at ScienceDirect

Journal of Science: Advanced Materials and Devices

journal homepage: www.elsevier.com/locate/jsamd

Original Article

First-principles studies of thermoelectric and thermodynamic properties of the complex perovskite $Ba_3MnNb_2O_9$

Saadi Berri [a, b, *]

[a] Laboratory for Developing New Materials and their Characterizations, University of Setif 1, Algeria
[b] Department of Physics, Faculty of Science, University of M'sila, 28000, M'sila, Algeria

ARTICLE INFO

Article history:
Received 29 March 2020
Received in revised form
5 May 2020
Accepted 15 June 2020
Available online 22 June 2020

Keywords:
Complex perovskite
Magnetic semiconductor
FP-LAPW
Thermoelectric
Thermal properties

ABSTRACT

The structural, electronic, magnetic, thermoelectric and thermodynamic properties of $Ba_3MnNb_2O_9$ have been investigated using the full-potential linearized augmented plane wave method. Besides, the thermodynamic properties of the materials of interest have been studied using the quasi-harmonic Debye model accommodating the lattice vibrations effects. A comparison between the computed crystal structure parameters and the corresponding experimental counterparts shows a very good agreement between them. The band structures (BS) and density of states (DOS) ensure the magnetic semiconductors nature of the studied complex perovskite. Moreover, the thermoelectric properties of this compound were studied using the transport quasi-classical theory. The effects of pressure and temperature on the studied properties are found to be highly effective in tuning some of the macroscopic properties of the compound in question.

1. Introduction

Perovskite-type materials have become very interesting in the field of photovoltaic devices [1–5]. A new generation perovskites of double perovskites have caused widespread concern because of their promising technological applications in the photovoltaic, photodetector or photocatalytic fields [6–8]. Among them, the complex perovskite oxides are versatile materials with trigonal structure and space group P-3m1 that show a wide variety of magnetic and electronic properties [9–12] which are related to the strong interplay between structure, charge and spin ordering. These materials found useful applications in the field of spin electronics [13]. As a matter of fact, spintronics is an emerging domain that will most likely have an important impact on the electronics aspects [14]. This is due to their amazing optical and electronic properties [15].

Half-metallic materials are those materials that act as conductors for electrons of one spin orientation, but as insulators or semiconductors for electrons of opposite spin orientation [16,17]. These materials have attracted much attention due to their potential use in spintronics [18,19]. Many studies investigated the half metallicity property in pervoskites, this is the due to the possibility of using such systems in spintronic applications. One of promising applications of spintronics is multiple-states memory devices, such as tunnelling magneto-resistance and giant magneto-resistence, whose functions totally depend on magnetization and can only be realized by using spin directon [20].

Moreover, structural, electrnic and magnetic properties of Sr_2GdReO_6 double perovskite were studied and the calculations predicted that Sr_2GdReO_6 is half-metallic, the ferromagnetic phase is found more favorable to occur [21]. In a very recent study the structural, electronic, and half–metallic properties of double perovskite $RBaMn_2O_{6-\delta}$ (X = Nd, Pr, La and δ = 0, 1) compounds were studied, the results show that they are half metallic ferromagnets [22]. Furthermore, the Sr_2XOsO_6 (X = Cs, Rb and K) compounds have been investigated theoretically, half-metallically is found in all the three compounds, all elastic constants "C_{ij}", the Shear moulus "G", Young modulus "E", Poisson ratio "ν", anisotropic factor "A" and Cauchy's pressure "C_{11}–C_{44}" for the studied compounds were also calculated [23].

The structural, electronic, thermoelectric and thermodynamic properties of solid materials are important fundamental parameters for an accurate understanding of the physics of solid state matter [24–26]. Under extreme conditions of temperature and pressure, the fundamental properties of solid materials behave in a manner different from that at normal conditions [27–29]. Thus, the

* Department of Physics, Faculty of Science, University of M'sila, 28000, M'sila, Algeria
E-mail addresses: berrisaadi12@yahoo.fr, saadi.berri@univ-msila.dz.
Peer review under responsibility of Vietnam National University, Hanoi.

https://doi.org/10.1016/j.jsamd.2020.06.002

Table. 1
Lattice constants *a* (Å) and *c* (Å), bulk modulus *B* (in GPa), first-pressure derivative of bulk modulus *B′*, individual, net magnetic moments (μ_B), energy band gap Eg.

$Ba_3MnNb_2O_9$	FP-LAPW	Exp
a(Å)	5.876	5.7698 [30] 5.8036 [38]
c(Å)	7.210	7.0855 [30] 7.0808 [38]
B (GPa)	152.87	–
B′	4.38	–
Eg (↑)	1.05	–
Eg (↓)	2.67	–
m_{Mn}	4.22373	4.4 [38]
m_{Ba}	0.00039	–
m_{Nb}	0.04996	–
m_O	0.00736	–
$m_{interstitial}$	0.44670	–
m_{Total}	5.00051	4.91 [38]

knowledge of the new properties of materials obtained under high temperature and pressure is extremely useful for the technological applications of these materials at extreme conditions.

However, only a limited data have been reported on the fundamental properties of $Ba_3MnNb_2O_9$ compound. This has motivated us to investigate on the structural, electronic, thermoelectric and thermodynamic properties of this material by performing the band structure calculations using the full-potential linear augmented plane wave (FP-LAPW) method within the generalized gradient approximation plus Hubbard parameter (GGA + U). The remaining of the paper is organized as follows: the theoretical background is described in Section 2. Results are presented and discussed in Section 3. A summary of the results is given in Section 4.

2. Method of calculation

As mentioned already, we have considered the experimental crystal parameters as reported by Liu et al. [30]. $Ba_3MnNb_2O_9$ compound crystallize in the trigonal space group P-3m1(No.164), Z = 1. The crystal structures of $Ba_3MnNb_2O_9$ compound is shown in Fig. S1. The crystal structures, are provided in the supplementary information S1. Band calculations are performed by using the full-potential linearized augmented plane wave (FP-LAPW) method [31] as implemented in WIEN2K code [32]. In the study of structural and electronic properties, the exchange correlation energy is treated within the GGA + U [33]. The effective Hubbard parameter $U_{eff} = U\text{-}J = 3$ eV was also applied to the 3d electrons of Mn ion. The mesh of K points in the first Brilluen zone by center of Γ point was selected to 15 × 15 × 13. We have chosen the lmax, RMTKmax and Gmax to be 10, 9 and 14, respectively. The thermoelectric properties of this $Ba_3MnNb_2O_9$ compound were calculated by applying Boltzman transport theory and BoltzTraP code [34]. To investigate the thermodynamic properties of $Ba_3MnNb_2O_9$ compound, we apply the quasi-harmonic Debye model [35]. Theoretical details of the model in question are available in Ref. [36] and references therein.

3. Results and discussion

The optimized lattice constants a and c, bulk modulus *B* and its pressure derivative *B′* at the equilibrium volume are calculated by fitting the total energy to Murnaghan's equation of state (EOS) [37]. Murnaghan's equation of state (EOS) is given by:

$$E(V) = E_0 + \frac{BV}{B'}\left[\frac{(V/V_0)^{B'}}{B'-1}+1\right] - \frac{BV_0}{B'-1} \quad (1)$$

where E_0 is the minimum energy. The pressure P and bulk modulus *B* are given by $p = -\frac{dE}{dV}, B = -V\frac{dP}{dV} = V\frac{d^2E}{dV^2}$. Fig. S2 shows the total energy as a function of the unit-cell volume (supplementary information SII). This has allowed the determination of *a*, *c*, *B* and *B'*. The resulting structural parameters for $Ba_3MnNb_2O_9$ compound being considered in the present work are listed in Table 1. Also shown for comparison are the available experimental data quoted in the literature. A good accord can be observed between our findings and the experimental data reported in Refs. [30,38] regarding *a*(Å) and *c*(Å) lattice parameters.

Investigations of the electronic band structure and the density of states are important because most of the physical properties of solids are related to them. The spin-polarized band structure in its tetragonal structure has been calculated using the FP-LAPW method. Based on the lattice symmetry, the integration paths P (0, 0, 0.5)- Γ(0, 0, 0)-N (0.5, 0.5, 0.5)-H (0, 0.5, 0.5)- Γ(0, 0, 0) are performed so as to treat the band structure for trigonal structre. The obtained results are plotted in Figs. 1–3.

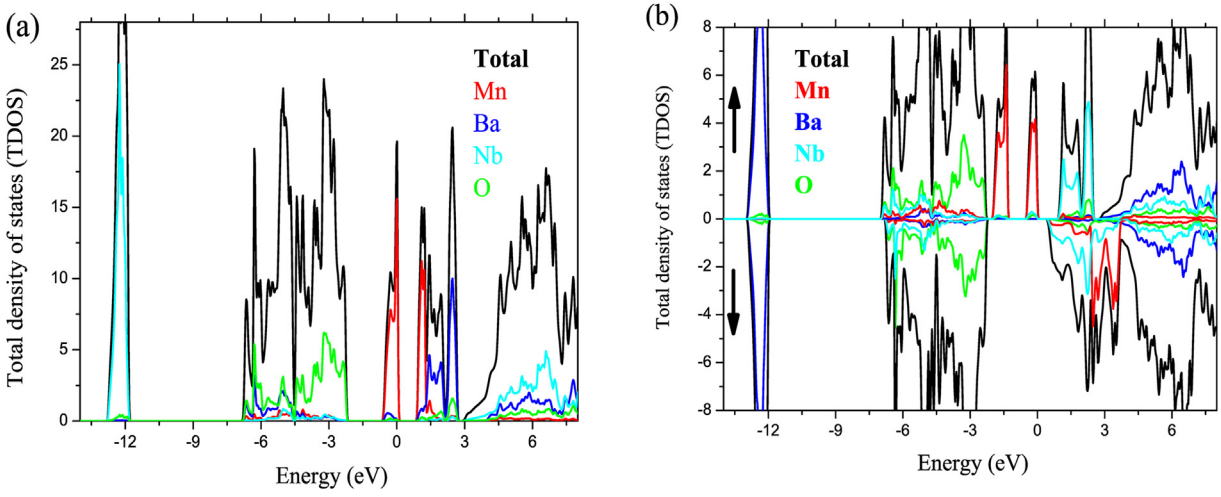

Fig. 1. Total densityof states (TDOS) for (a) non-magnetic and (b) ferromagnetic state.

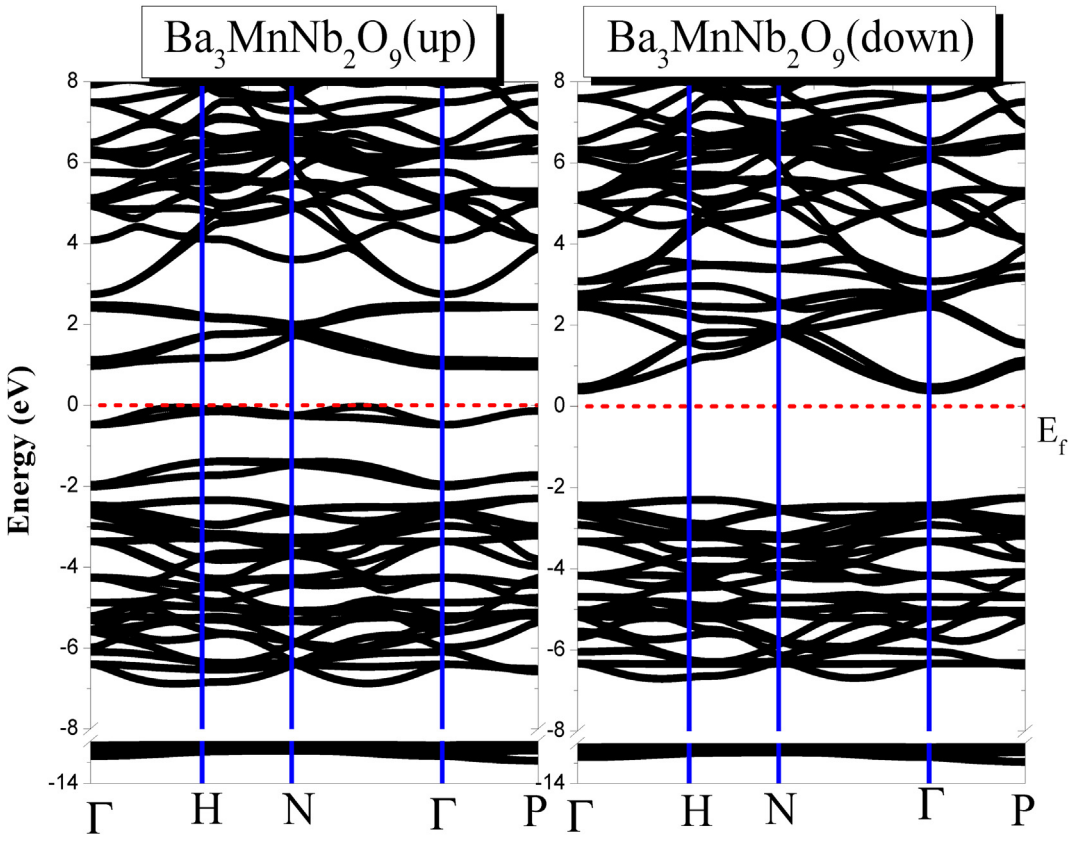

Fig. 2. Band structure for high-symmetry directions in the Brillouin zone for $Ba_3MnNb_2O_9$.

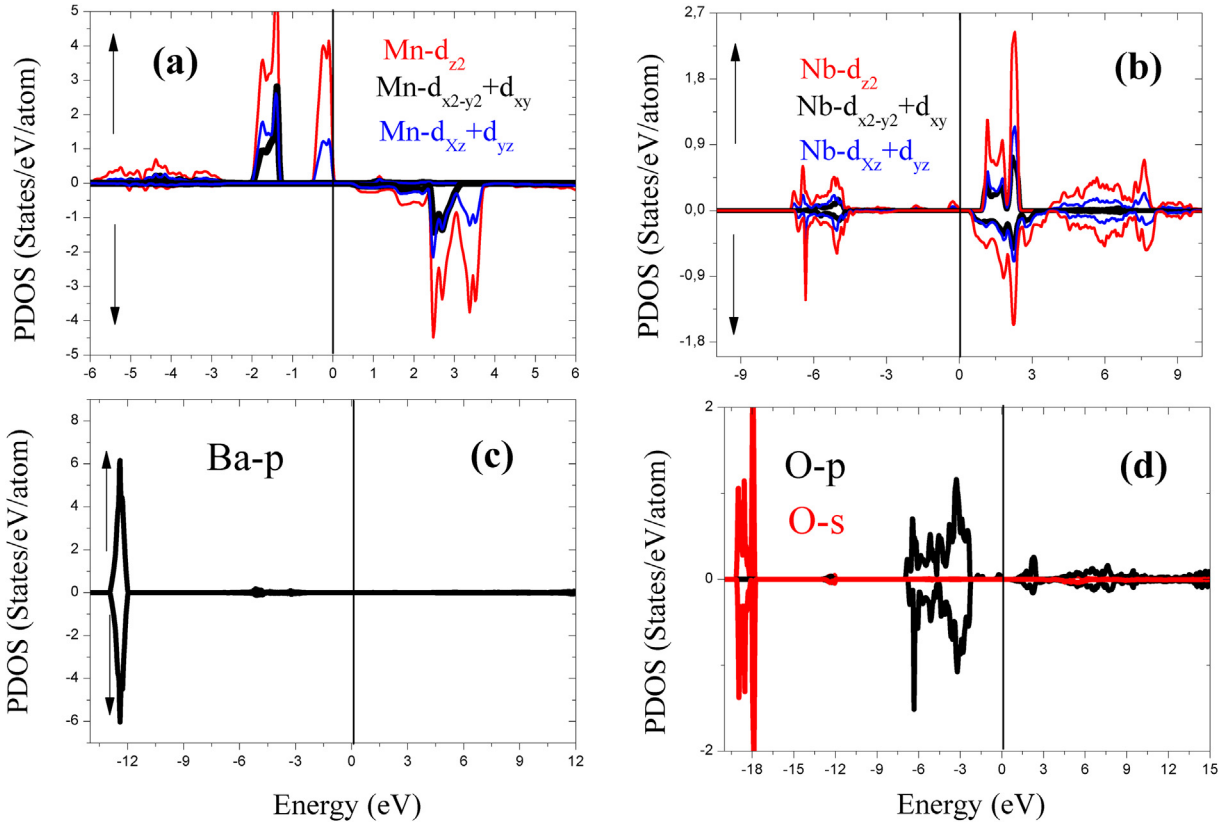

Fig. 3. Projected density of states for $Ba_3MnNb_2O_9$ compound a) Mn-(d_{z2}, $d_{X2-Y2}+d_{XY}$ and $d_{XZ}+d_{YZ}$), b) Nb-(d_{z2}, $d_{X2-Y2}+d_{XY}$ and $d_{XZ}+d_{YZ}$), c) Ba-p and d) O-(s, p).

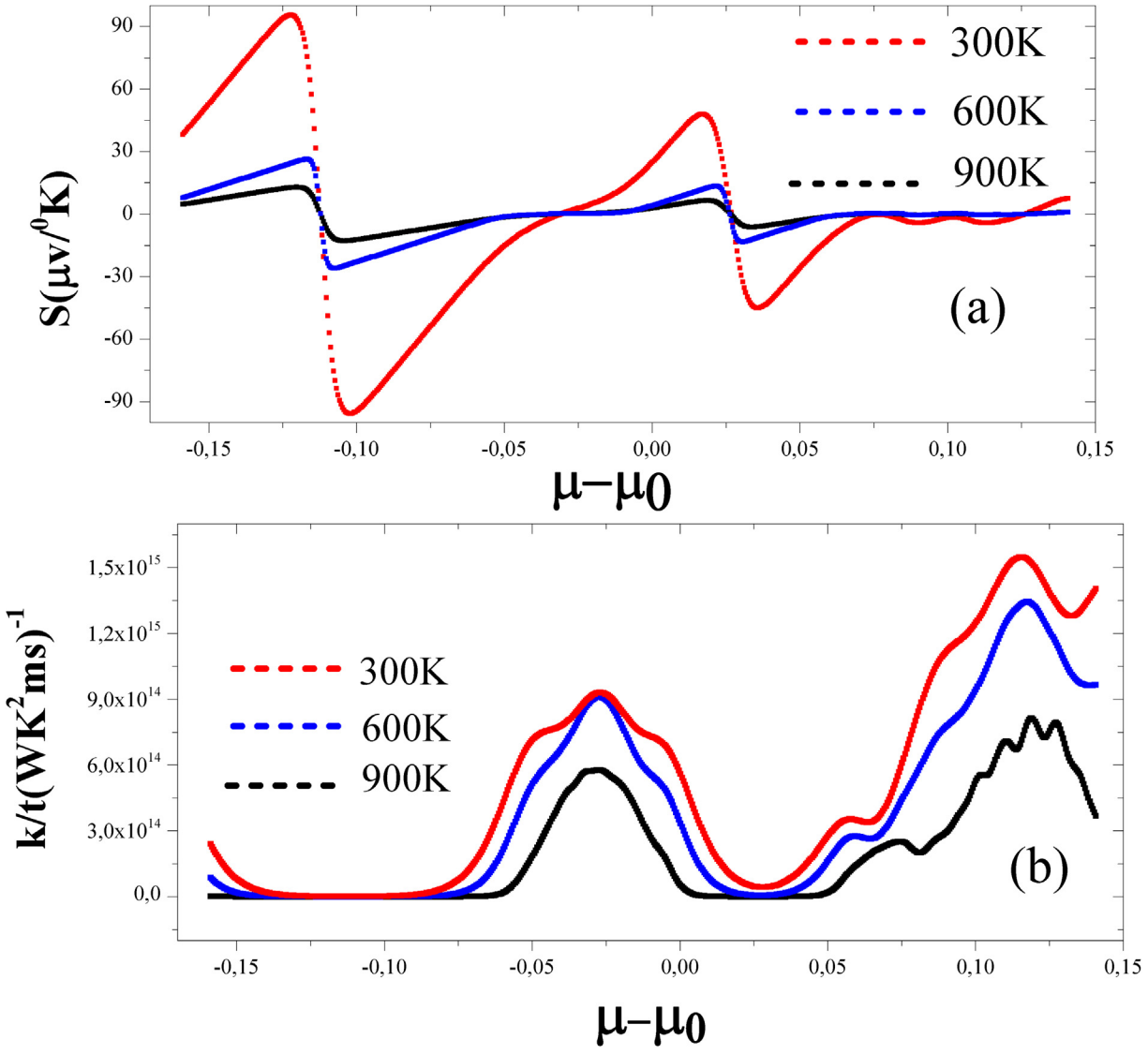

Fig. 4. Calculated (a) Seebeck coefficient and (b) Electrical conductivity against the chemical potential.

Fig. 3 shows the calculated total density of states (TDOS) of perfect $Ba_3MnNb_2O_9$ in the non-magnetic (NM) and ferromagnetic state, the Fermi level is regarded as reference zero point.

The calculated spin-polarized band structure and density of states of spin-up (majority spin) and spin-down (minority spin) of $Ba_3MnNb_2O_9$ are depicted in Figs. 1 and 3, respectively. For ferromagnetic case show an indirect band-gap of 3.23 eV in the spin-down channel with valence band maximum (VBM) being −2.23 eV at P points and conduction band minimum (CBM) being 0.48 eV at Γ point with wide semiconducting gap. For spin-up case, both VBM and CBM were pushed up to 0.00 eV and 1.00 eV, respectively, slightly reducing the direct band-gap at P point to 1.00 eV. Similar band structure have been observed for $CaCu_3Ge_4O_{12}$ compound calculated with a full-potential linearized augmented plane wave method [39].

The calculated energy band gap in both spin are listed in Table 1. In order to get a deeper insight into the electronic structure of $Ba_3MnNb_2O_9$, the partial densities of states (PDOS) have been calculated in both the majority and minority spin (See Fig. 3). The Fermi level is set as 0 eV. As can be seen from Fig. 3, the DOS can be divided into four parts, at lower energy where (below −12.0 eV) we find the contribution of Ba p and O s states; the second part is from −6 eV to −3 eV that is mainly derived from O p states; the third part which is beyond the Fermi level, is essentially contributed by the d_{z2}, d_{X2-Y2}+d_{XY} and d_{XZ} + d_{YZ} of Mn atoms; the conduction region is mainly contributed by the s state of d_{z2}, d_{X2-Y2}+d_{XY} and d_{XZ} + d_{YZ} of Nb atoms.

The obtained total, interstitial and atom-resolved magnetic moments of $Ba_3MnNb_2O_9$ are shown in the Table 1. For $Ba_3MnNb_2O_9$, the total magnetic moment agrees with recent experimental data [38]. The principal contribution to the total magnetic moment comes from the Mn atoms and small contributions from the interstitial region, whereas the moments of Ba, Nb and O are small. The magnetic moments of the Mn atoms (Table .1) shows agreement with the experiment as quoted in Ref [38]. The exchange-splitting between the spin-up and spin-down sub-bands of the Mn d_{z2}, d_{X2-Y2}+d_{XY} and d_{XZ} + d_{YZ} states is the main contributor in the magnetic moment of $Ba_3MnNb_2O_9$ compound.

In the next stage, we presented the thermoelectric parameter diagrams of the $Ba_3MnNb_2O_9$ compound including the Seebeck coefficient (S), the electrical conductivity (σ), the electronic thermal conductivity (Kel) and the figure of Merit (ZT) in Fig. 4.

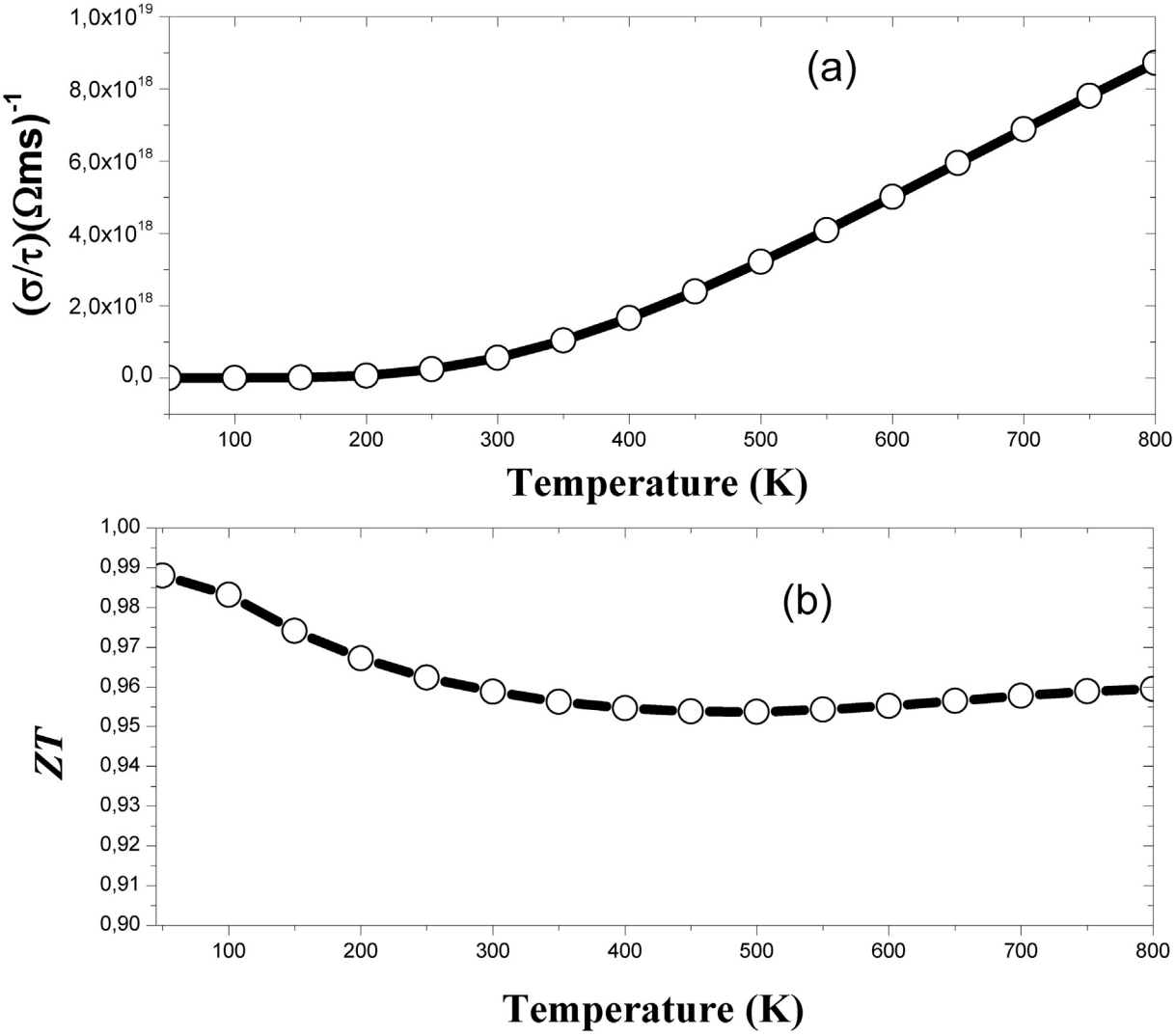

Fig. 5. Calculated (a) electrical thermal conductivity and (b) merit (ZT) as a function of temperature.

Fig. 4(a) shows the Seebeck effect of $Ba_3MnNb_2O_9$ compound. the Seebeck effect takes place as a result of the temperature gradient across a thermoelectric material. The mobility of charge carriers triggered by the temperature difference results in the voltage gradient which is considered as the main principle of thermoelectric power generation. Seebeck coefficient holds inverse relationship the σ/τ and are therefore strongly influenced by the size and nature of bandgap as well as the effective mass of the charge carriers. The major Seebeck coefficients occur corresponding to the separation between the valence and conduction band edges due to the reduced density of charge carriers corresponding to the energy bandgap.

The electrical conductivity against chemical potential at 300 K, 600 K and 900 K temperature are plotted in Fig. 4(b). It is clear from the figure that for different temperatures, the magnitude of the electrical conductivity increases with the increase of absolute values of the chemical potential; and the high value of electrical conductivity is observed in the positive range of chemical potential. On the other hand, It is clear that the thermal conductivity (see Fig. 5(a)) at room temperature is lower than those corresponding to 450 and 900 K, so the thermal properties of this compound is also completely sensitive to the external magnetic field.

Dimensionless figure of Merit (ZT) is the most important thermal transport parameters that can be used to determine the thermal efficiency of compounds. In Fig. 5(b), in general at all temperatures the ZT coefficient is a very slight number especially at temperatures from 50 to 100K. We observe that at temperatures below room temperature the ZT value is about 0.99 so in comparison with other values of the figure of Merit at the room temperature in the previous theoretical and experimental studies, such as: NiTiSn [40] and CuI–Pb co-doped Bi_2Te_3(ZT = 0.96) [41] it can be concluded that this compound will be very suitable for application in the thermoelectric cooling industry. With increasing temperature the amount of ZT has decreased but it is important to note that this value is about 0.95 at room temperature which is still significant. Even in 800K the figure of Merit has an acceptable extent so this compound has also the ability to use in power generators.

The thermodynamic properties of $Ba_3MnNb_2O_9$ compound under high pressure and at different temperatures have been determined using the quasi-harmonic Debye approximation. As a first step, a set of total energy calculations versus primitive cell volume (E–V) is carried out, in the static approximation. The results are then fitted with a numerical EOS so as to determine the structural parameters at P = 0 and T = 0, and to derive the macroscopic properties as a function of pressure and temperature from standard

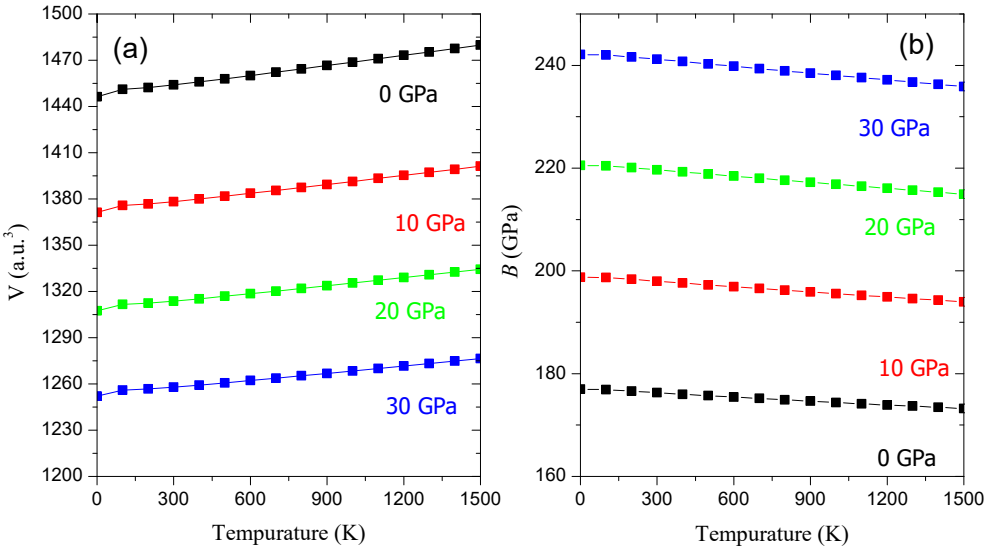

Fig. 6. Temperature dependence of (a) volume and (b) Bulk modulus *B* at various pressures.

thermodynamic relations. The diagrams which show the volume unit cell-temperature at various pressures and lattice parameter-pressure at different temperatures for $Ba_3MnNb_2O_9$ compound being considered in this work are plotted in Fig. 6(a). We observe that for a given pressure, the volume unite cell increases monotonically with increasing temperature. Nevertheless, the rate of increase appears to be very moderate. On the other hand, for a given temperature, the volumes unite cell decreases with applying pressure. In the present contribution, the calculated volumes for $Ba_3MnNb_2O_9$ compound at zero pressure and room temperature is found to be 1453.98 (u.a.)^3.

Fig. 6(b) displays the temperature dependence of *B* at various pressures for $Ba_3MnNb_2O_9$ compound. Note that all the relationships between *B* and temperature are almost linear at various pressures ranging from 0 to 30 GPa. As a matter of fact, *B* decreases monotonically and very moderately when the temperature is increased. At room temperature and zero pressure, *B* for $Ba_3MnNb_2O_9$ compound is found to be 176.29 GPa. This value is in reasonably good accord with those obtained in the current work using FP-LAPW method (see Table 1).

The variation of the heat capacity at a constant volume C_V as a function of temperature at various pressures ranging from 0 to 30 GPa for $Ba_3MnNb_2O_9$ compound is shown in Fig. 7(a). We observe that C_V augments at elevated temperatures. The behavior seems to be quick at low temperatures but becomes slower at elevated temperatures. For temperatures less than 500 K, C_V depends on both temperature and pressure. At high temperatures, C_V approaches approximately 371.24 $Jmol^{-1}K^{-1}$ for $Ba_3MnNb_2O_9$ compound. The details in the change appear to depend on pressure. The behavior of C_V for this compound of interest exhibits similar features in a wide range of pressures and temperatures.

The temperature dependence of the thermal expansion coefficient α of the $Ba_3MnNb_2O_9$ compound at various pressures are depicted in Fig. 7(b), it is clear that below 600 K, the thermal

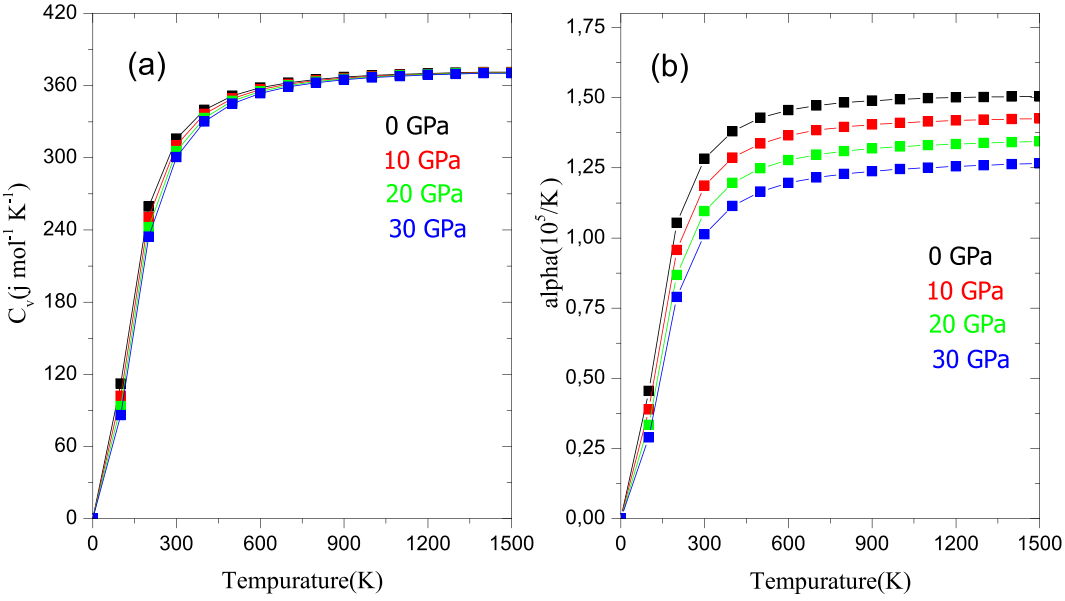

Fig. 7. Temperature dependence of (a) heat capacities Cv and (b) thermal expansion coefficient α at various pressures.

expansion coefficient increases rapidly, whereas at temperatures higher than 600 K, the α value initially remains constant and then increases linearly at high pressure. At zero pressure and T = 300 K, α takes the values of $1.28 \times 10^{-5}K^{-1}$.

4. Conclusion

In summary, based on first-principle calculations in the framework of DFT within the GGA + U, the structural, electronic, magnetic, thermoelectric and thermodynamic properties of trigonal $Ba_3MnNb_2O_9$ were investigated. Special attention was given to the effects of temperature and pressure on these features. The optimized lattice parameters are found to be in good accord with experiment. Features such as bulk modulus and its pressure derivative, electronic band structure and density of states are reported. The electronic band structures as well as density of states reveal that the studied compound shows magnetic semiconductor behavior under ambient conditions. Moreover, the novelty of our work is the study of thermoelectric properties of $Ba_3MnNb_2O_9$ complex perovskite such as Seebeck coefficient, electrical conductivity, electrical thermal conductivity and merit. The thermal effects on the macroscopic properties of the compound of interest were predicted and discussed using the quasi-harmonic Debye model where the lattice vibrations were taken into consideration.

Declaration of Competing Interest

The author declares no conflict of interests.

Appendix A. Supplementary data

Supplementary data to this article can be found online at https://doi.org/10.1016/j.jsamd.2020.06.002.

References

[1] A. Kojima, K. Teshima, Y. Shirai, T. Miyasaka, Organometal halide perovskites as visible-light sensitizers for photovoltaic cells, J. Am. Chem. Soc. 131 (2009) 6050.
[2] F. Robert, Service, Energy technology. Perovskite solar cells keep on surging, Science 344 (2014) 458.
[3] H.J. Snaith, Perovskites: the emergence of a new era for low-cost, high-efficiency solar cells, J. Phys. Chem. Lett. 4 (2013) 3623.
[4] P. Tonui Saheed, O. Osenia, Gaurav Sharma, Qingfenq Yan, Perovskites photovoltaic solar cells: an overview of current status, Renew. Sustain. Energy Rev. 91 (2018) 1025.
[5] K.T. Butler, J.M. Frost, A. Walsh, Band alignment of the hybrid halide perovskites CH3NH3PbCl3, CH3NH3PbBr3 and CH3NH3PbI3 Mater, Horizon 2 (2015) 228, and references therein.
[6] J. Yang, P. Zhang, S.-H. Wei, Band structure engineering of Cs2AgBiBr6 perovskite through order–disordered transition: a first-principle study, J. Phys. Chem. Lett. 9 (2018) 31.
[7] R. Fu, Y. Chen, X. Yong, Z. Ma, L. Wang, P. Lv, S. Lu, G. Xiao, B. Zou, Pressure-induced structural transition and band gap evolution of double perovskite $Cs_2AgBiBr_6$ nanocrystals, Nanoscale 11 (2019) 17004.
[8] G. Garcia-Espejo, D. Rodriguez-Padrón, R. Luque, L. Camacho, G. de Miguel, Mechanochemical synthesis of three double perovskites: $Cs_2AgBiBr_6$, $(CH_3NH_3)_2TlBiBr_6$ and $Cs_2AgSbBr_6$, Nanoscale 11 (2019) 16650.
[9] C. D Ling, M. Avdeev, R. Kutteh, V.V. Kharton, A.A. Yaremchenko, S. Fialkova, N. Sharma, R. B Macquart, M. Hoelzel, M. Gutmann, Structures, phase transitions, hydration, and ionic conductivity of Ba4Nb2O9, Chem. Mater. 21 (16) (2009) 3853.
[10] M.T. Dunstan, P.D. Southon, C.J. Kepert, J. Hester, J.A. Kimpton, C.D. Ling, Phase diagram, chemical stability and physical properties of the solid-solution $Ba_4Nb_2-xTaxO_9$, J. Sol. State. Chem. 184 (10) (2011) 2648.
[11] J.E.F.S. Rodrigues, D.M. Bezerra, A.R. Paschoal, A.P. Maciel, C.W. de A. Paschoa, Probing phase formation and structural ordering in Ba3ZnNb2O9 films using confocal Raman microscopy, Vib. Spectrosc. 72 (2014) 8.
[12] Md.M. Hoque, A. Dutta, S. Kumar, T.P. Sinha, Structural and dielectric properties of $Sr_3(MgTa_2)O_9$ and $Sr_3(ZnTa_2)O_9$, Phys. B Condens. Matter 468–469 (2015) 85.
[13] H. Kato, T. Okada, Y. Okimoto, Y. Tomioka, K. Oikawa, T. Kamiyama, Y. Tokura, Structural and electronic properties of the ordered double perovskites A2MReO6 (A=Sr,Ca; M=Mg,Sc,Cr,Mn,Fe,Co,Ni,Zn), Phys. Rev. B 69 (2004) 184412.
[14] S.A. Wolf, D.D. Awschalom, R.A. Buhram, J.M. Daughton, S. van Molnár, M.L. Roukes, A.Y. Chtchelkanova, D.M. Treger, Spintronics: A Spin-Based Electronics Vision for the Future Science 294 (2001) 1488.
[15] S. Parkin, X. Jiang, C. Kaiser, A. Pan chula, K. Roche, M. Samant, Magnetically engineered spintronic sensors and memory Proc, High Perform. Dev. IEEE Cornell Conf. 91 (2003) 5.
[16] R.A. de Groot, F.M. Mueller, P.G. Van Engen, K.H.J. Buschow, New class of materials: half-metallic ferromagnets, Phys. Rev. Lett. 50 (1984) 2024.
[17] K. Sato, L. Bergqvist, J. Kudrnovský, P.H. Dederichs, O. Eriksson, I. Turek, B. Sanyal, G. Bouzerar, H. Katayama-Yoshida, V.A. Dinh, T. Fukushima, H. Kizaki, R. Zeller, First-principles theory of dilute magnetic semiconductors, Rev. Mod. Phys. 82 (2010) 1633.
[18] L. Bansla, M.M. Raja, A.K. Nigam, K.G. Suresh, CoRuFeX (X = Si and Ge) heusler alloys: High TC materials for spintronic applications, J. Alloys. Comp 651 (2015) 635.
[19] S. Berri, The electronic structure and spin polarization of Co2Mn0.75(Gd, Eu) 0.25Z (Z=Si, Ge, Ga, Al) quaternary Heusler alloys, J. Magn. Magn Mater. 401 (2016) 667.
[20] H.K. Yoshida, K. Sato, T. Fukushima, M. Toyoda, H. Kizaki, A.V. Din, H.P. Dederichs, Theory of ferromagnetic semiconductors, Phys. Status Solidi 204 (2007) 15.
[21] S. Berri, First-principles study on half-metallic properties of the Sr_2GdReO_6 double perovskite, J. Magn. Magn Mater. 385 (2015) 124.
[22] S. Berri, N. Bouarissa, M. Attallah, First-Principles predictions on half-metallic results of $RBaMn_2O_{6-\delta}$ (R = Nd, Pr, La and δ = 0, 1) double perovskite compounds, J. Supercond. Nov. Magnetism (2020), https://doi.org/10.1007/s10948-020-05426-0.
[23] M. Faizan, G. Murtaza, S.H. Khan, A. Khan, A. Mehmood, R. Khenata, S. Hussain, First-principles study of the double perovskites Sr2XOsO6 (X = Li, Na, Ca) for spintronics applications, Bull. Mater. Sci. 39 (6) (2016) 1419.
[24] C. Li, N.K. Ravichandran, L. Lindsay, D. Broido, Fermi surface nesting and phonon frequency gap drive anomalous thermal transport, Phys. Rev. Lett. 121 (2018) 175901.
[25] X. Yang, C. Peng, L. Li, M. Bo, Y. Sun, Y. Huang, C.Q. Sun, Multifield resolved phonon spectrometrics: structured crystals and liquids, Prog. Solid State Chem. 55 (2019) 20.
[26] C.C. Rinzler, A. Allanore, A thermodynamic basis for the electronic properties of molten semiconductors: the role of electronic entropy, Philos. Mag. A 97 (2017) 561.
[27] A. Mujica, A. Rubio, A. Muñoz, R.J. Needs, High-pressure phases of group-IV, III–V, and II–VI compounds, Rev. Mod. Phys. 75 (2003) 863.
[28] I.I. Shpak, I.I. Rosola, O.I. Shpak, Temperature dependence of the refractive index of glassy alloys of the AsxS100–x system, J. Appl. Spectrosc. 84 (2017) 140.
[29] K. Daviau, K.K.M. Lee, High-pressure, high-temperature behavior of silicon carbide: a review, Crystals 8 (2018) 217, and references therein.
[30] Y. Liu, R.L. Withers, A.P. Whichello, L. Noren, V. Ting, F. Brink, J.D.F. Gerald, A combined diffraction and dielectric properties investigation of Ba3MnNb2O9 complex perovskites, J. Solid State Chem. 178 (11) (2005) 3389.
[31] P. Blaha, K. Schwarz, P. Sorantin, S.B. Trickey, Full-potential, linearized augmented plane wave programs for crystalline systems, Comput. Phys. Commun. 59 (1990) 399.
[32] P. Blaha, K. Schwarz, G.K.H. Medsen, D. Kvasnicka, J. Luitz, in: Karlheinz Schwartz (Ed.), An Augmented Plane Wave Local Orbitals Program for Calculating Crystal Properties, WIEN2k, Techn. Universitad, Wien, Austria, 2001.
[33] C. Loschen, J. Carrasco, K.M. Neyman, F. Illas, First-principles LDA+U and GGA+U study of cerium oxides: dependence on the effective U parameter, Phys. Rev. B 75 (2007) 035115.
[34] G.K.H. Madesan, D.J. Sing, BoltzTraP. A code for calculating band-structure dependent quantities Comput, Phys. Commun. 175 (2006) 67.
[35] M.A. Blanco, E. Francisco, V. Luaña, GIBBS: isothermal-isobaric thermodynamics of solids from energy curves using a quasi-harmonic Debye model comput, Phys. Commun. 158 (2004) 57.
[36] S. Berri, First-principles calculations to investigate structural, electronic, half-metallic and thermodynamic properties of hexagonal UX2O6 (X=Cr,V) compounds, J. Sci.: Adv. Material. Dev. 4 (2) (2019) 319.
[37] F.D. Murnaghan, The compressibility of media under extreme pressures, Proc. Natl. Acad. Sci. U.S.A. 30 (1944) 244.
[38] M. Lee, E.S. Choi, X. Huang, J. Ma, C.R. Dela Cruz, M. Matsuda, W. Tian, Z.L. Dun, S. Dong, H.D. Zhou, Magnetic phase diagram and multiferroicity of Ba3MnNb2O9: a spin-5/2 triangular lattice antiferromagnet with weak easy-axis anisotropy, Phys. Rev. B 90 (2014) 224402.
[39] H. Shiraki, T. Saito, T. Yamada, M. Tsujimoto, M. Azuma, H. Kurata, S. Isoda, M. Takano, Y. Shimakawa, Ferromagnetic cuprates CaCu3Ge4O12 and CaCu3Sn4O12 with A-site ordered perovskite Structure, Phys. Rev. B 76 (2007) 140403 (R).
[40] A. Berche, P. Jund, Fully Ab-initio determination of the thermoelectric properties of half-heusler NiTiSn: crucial role of interstitial Ni defects, Materials 11 (2018) 868.
[41] Mi-Kyung Han, Yingshi Jin, Da-Hee Lee, Sung-Jin Kim, Thermoelectric Properties of Bi2Te3 Materials 10 (2017) 1235.